# Designing CEDAR : Conversion Electron Detection ARray

**Samuel Hallam**

A dissertation submitted to the Physics Department at the University of Surrey in partial fulfilment of the degree of Master in Physics.

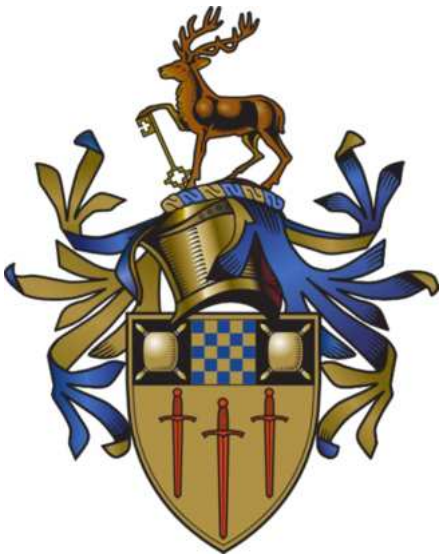

Department of Physics,

Faculty of Engineering and Physical Sciences,

University of Surrey, Guildford, Surrey, GU2 7XH

Jan 2016

# Abstract

Conversion electron spectrometers have been designed in various ways at many different facilities in order to further our knowledge of the nucleus and its structure. The goal of this masters was to design an upgrade to the PACES array (that has been previously used in the $8\pi$ $\gamma$-ray spectrometer) to be used in the new state-of-the-art GRIFFIN decay station, allowing coincidence measurements of $\gamma$ rays and conversion electron transitions.Before construction, a series of Geant-4 simulations are planned in order to design an array which will fit within the target chamber of GRIFFIN and then to optimize this designed array in order to maximize the peak efficiency, count rate and background reduction of the detector. The design of this detector will be based on many previous designs that have been built and tested. It is planned to use a permanent magnetic lens in order to bend electrons onto a cryogenically cooled lithium drifted silicon detector. The lens will be coupled to a photon shield.

# Acknowledgements

I would like to extend my gratitude to Dr. A. B. Garnsworthy, Dr. M. Moukaddam, Dr. J. Smallcombe and Mr. L. J. Evitts for their support throughout this project. I would also like to thank the Gamma-Ray Spectroscopy group based at TRIUMF. A special thank you to Dr. P. Stevenson from the University of Surrey for organising this placement.

# List of Figures

# List of Tables

# Contents

# Chapter 1

# Introduction & Background

TRIUMF is Canada's National Laboratory for Nuclear and Particle Physics. It is home to the largest cyclotron in the world, which accelerates negatively charged hydrogen ions up to 500 MeV of energy (75% speed of light). The H- ions are injected into two semi-circular chambers, within two large circular electromagnets. An alternating voltage is applied across these chambers in order to accelerate the ions. Passed through a graphite foil when a specified energy is reached, the ions are stripped of electrons leaving just protons. As the protons are positively charged they are bent out of the cyclotron by the magnetic field. These can then be simultaneously fed into four different beam lines heading to various facilities within TRIUMF, including nuclear medicine facilities (medical isotope production or proton cancer therapy), irradiation testing of electronic circuits and a materials science facility [1].

Of particular interest is the beam line serving the ISAC (Isotope Separator and ACcelerator) facility. Here the proton beam (of an energy of 475-500 MeV) is directed onto a target material, such as uranium-carbide. Within this target the processes of fission, fragmentation and spallation produce various rare-isotope beams (RIBs) [2]. Isotopes of interest are then separated using the ISOL (Isotope Separation On-Line) technique, these are then delivered to one of various experimental set-ups within the ISAC facility [3]. The isotopes are delivered to experimental set-ups either through a superconducting linear accelerator, for the ISAC-II hall, or by the LEBT (Low-Energy Beam Transport) electrostatic beam line for the ISAC-1 experimental area.

The GRIFFIN (Gamma-Ray Infrastructure For Fundamental Investigation of Nuclei) array is composed of 16 HPGe (High Purity Germanium) semiconducting clover

detectors. As a state-of-the-art decay station it measures $\gamma$ rays following the decay of RIBs which are slowed and implanted onto a Mylar tape in the centre of the array. These will help to investigate near stability nuclei and the most neutron rich nuclei, using very high statistics. With an array of ancillary detectors, the branching ratios and half-lives of Fermi super-allowed beta emitters near N=Z can also be measured with more accuracy than previously achieved [3].

SCEPTAR (SCintillating Electron-Positron Tagging ARray), originally the vacuum chamber for the $8\pi$ array, is now used in conjunction with GRIFFIN. The array contains 20 plastic scintillator paddles, split into two hemispheres of 10, with the purpose of tagging beta decay particles from radioactive sources [3] and [4]. This allows investigations of the end-point energies of these decays and can be used as a powerful coincidence filter, increasing the sensitivity of GRIFFIN measurements.

CEDAR is planned as an ancillary detector. It will form the upstream hemisphere of the target chamber (SCEPTAR) that lies within the GRIFFIN HPGe array. The detector will measure the energy of Internal Conversion Electrons (ICEs), allowing $\gamma - e^-$ coincidences that will allow the observation of transitions and branching ratios of states within a nucleus. It will also be used to measure *E0* transitions between $0^+$ states which is important in the measurement of branching ratios of a parent state. In order to do this a detector with a high count rate capability, a wide energy acceptance of electrons and a high transmission efficiency will be designed. It must also not hamper the efficiency of GRIFFIN.

# Chapter 2

# Internal Conversion Spectrometers

The typical design of conversion electron spectrometers involves a combination of two devices, one for transportation of electrons and for one for their detection. Either to guide them around a physical barrier or over a large distance from a target. The following designs were taken into account in the design of the new detector.

## 2.1 Momentum Selective Solenoids

Electron spectrometers have previously been designed to utilize solenoidal lenses with large electrical currents. These lenses produce a magnetic field that is parallel to the motion of electrons from the source to the semiconductor detector. Helical baffles are placed within the device and combined when with a varying current in a solenoid (and therefore the magnetic field strength) a select momentum window of electrons is created (only electrons within this window will have a helical path that passes through the baffles). The baffles absorb positrons emitted from a source, which follow the same but directionally opposite helical pattern due to the magnetic field. Photon shielding reduces the background from $\gamma$ rays. The detector is placed at a tangent to the source and electrons hit the face after one half period of motion. Consequently a limited momentum window (between $\Delta p/p = 0.1 - 0.4$) can be observed at one time, by sweeping across momentum windows large ranges or electron energy can be observed. An example of this is Siegbahn-Kleinheinz spectrometer. However, this reduces the count rate achievable, statistically problematic for time limited experiments [5], [6] and [7].

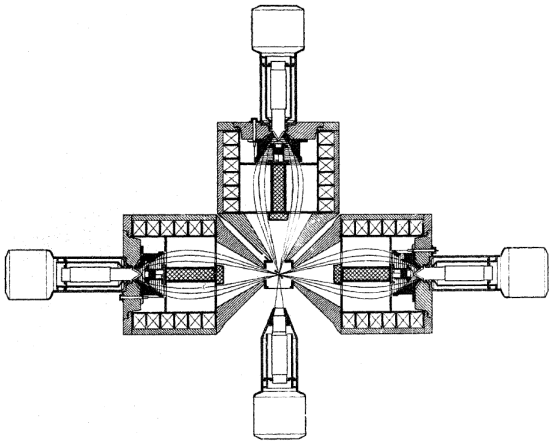

***Figure 2.1:*** *Cross section schematic of the electron directional correlation spectrometer. Showing three devices placed around a source of conversion electrons. The figure also depicts the helical path of the electrons around a photon shield onto a detector. [5]*

## 2.2 Large Momentum Acceptance Solenoids

Like the momentum selective detectors these utilize solenoids (superconducting or otherwise) to produce helical trajectories of electrons through a parallel magnetic field. The key difference between the designs of momentum selective devices and large acceptance devices is that these arrays implement an increased target-to-detector distance in order to reduce the amount of background in the detector. This distance allows for many oscillations of the electrons before entering the detector and the removal of the helical baffles and photon shield. This gives them a larger window of acceptance. These detectors work only in the backwards angle and to further reduce the background from the $\delta$ particles, (from heavy ion interactions) they implement a high voltage barrier (up to 50 kV) near to the detector. Examples of these detectors are the SACRED (Solenoid and Array for ConveRsion Electron Detection) and SAGE (Silicon And GErmanium) spectrometers at the University of Jyväskylä [8] and [9]. Both are used for measuring low energy electrons from heavy isotopic studies. SAGE has an absolute efficiency of 9% at 300 keV using a 30 kV HV barrier. A large problem with these designs is that when used in conjunction with $\gamma$-ray spectrometers the large uncontained field from the solenoids can interfere with photomultiplier tubes within bismuth germanate suppressors (BGOs), such as those planned for use in GRIFFIN. SAGE has overcome the problem from the magnetic field with its $\gamma$-ray spectrometer

by shielding the BGOs with a steel cylinder distorting the field enough to allow full function.

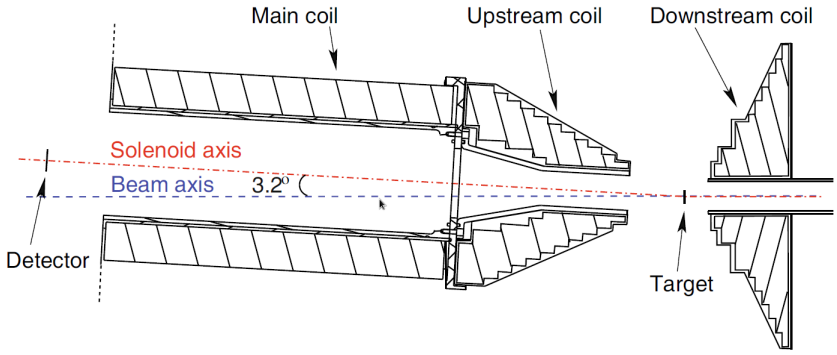


***Figure 2.2:*** *Cross section schematic of the SAGE spectrometer. The figure shows the extended distance between the target and detector. Also shows the solenoidal coils. [9]*

## 2.3 Semiconductor Array Spectrometers

These spectrometers are rather simple in their design. They contain an array of detectors such as lithium drifted silicon semiconductors placed in close proximity to a target. There is no use of a magnetic field, photon shield or a HV barrier in these designs and so nothing is done to prevent background radiation. The efficiency is dependent only on the solid angle occupied by the detector array and the energy range in which they are effective at is dependent on the thickness of the detector. An example of a design like this is PACES (Pentagonal Array for Conversion Electron Spectroscopy) in which a 5% absolute efficiency can be achieved up to 2 MeV (due to the 5 mm thickness of the detector array). The main issue of a design like this is that there is a large amount of background in the data collected. As there is no background reduction in these devices, all radiation emitted will be detected. Conversion electron peaks typically have small branching ratios in comparison to other radiation and so peaks in the data can be drowned out. Also in particular for PACES there is a very low count rate due to having only 5 Si-Li detector components. [4].

## 2.4 Permanent Magnet Spectrometers

Permanent magnet spectrometers do not use solenoids in order to transport electrons onto a detector; instead they employ permanent magnets to create a magnetic field that is perpendicular to the beam axis and the motion of the electrons from the target to detector. This looks like a circular magnetic field across the x-y plane if the z-axis is taken to be the beam axis. The electrons are bent towards the centre of the field, where a detector can be placed (perpendicular to the beam axis) and then shielded from $\gamma$ rays with a high effective proton number material. This means the magnetic field bends the electrons around this photon shielding. The classic design of this is commonly referred to as the "mini-orange" set up and uses wedge shape magnets in order to create the necessary field. This set up is sufficiently compact to fit within the target chamber of a $\gamma$-ray spectrometer [10]. ICEBALL uses 6 such devices to achieve a peak efficiency of 15% at 400 keV, dropping to 5% at 900 keV [11]. There are a few major disadvantages of older permanent magnet designs. They have relatively small energy acceptance windows, especially around peak efficiency. Also, the amount of material within the detector reduces the efficiency of any co-used $\gamma$-ray spectrometers, as well as increasing the number of scattered electrons and $\gamma$ rays which can be detected.

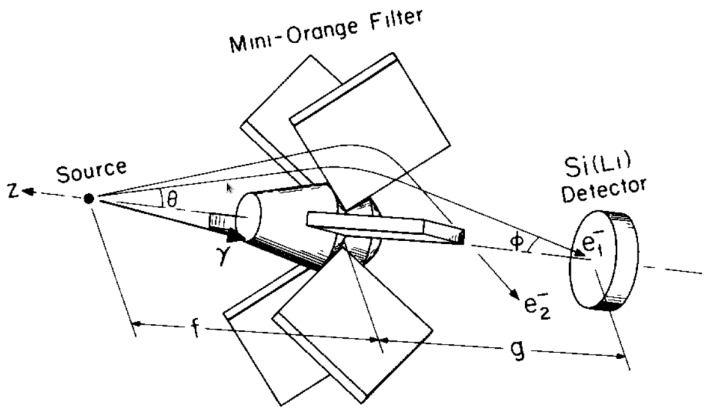


***Figure 2.3:*** *Schematic of one ICEBALL mini-orange array. The figure shows the trajectories of a selection of radiation, as well as the layout of the detector components. [10]*

A more recent variation of these detectors was designed at TRIUMF. Instead of using a wedge shaped magnet design, SPICE (SPectrometer for Internal Conversion Electrons) employs a paddle shaped magnet design consisting of three separate plates

(one thinner, longer middle plate with two thicker, shorter outer plates) with a "cut" on the source facing side of the middle plate. SPICE has managed to surpass efficiencies and energy acceptance windows of previous iterations of these permanent magnet designs. It has 3 different magnetic lenses which give rise to different ranges of energy acceptance. These include a "low-energy lens" (with a peak efficiency of 20% at 300 keV dropping to 5% at 900 keV), a "medium-energy lens" (peak efficiency of 16% at 800 keV dropping to 5% at 1.5 MeV) and a "high-energy lens" (peak efficiency of 12% at 2.8 MeV dropping to 5% at 3.7 MeV) [12]. A disadvantage of SPICE is that the design is not compact enough so that all 16 HPGe detectors can fit inside the TIGRESS (TRIUMF-ISAC Gamma-Ray Escape Suppressed Spectrometer) array, which it is used in combination [13]. Instead 4 of the HPGe detectors need to be removed before SPICE can be used.

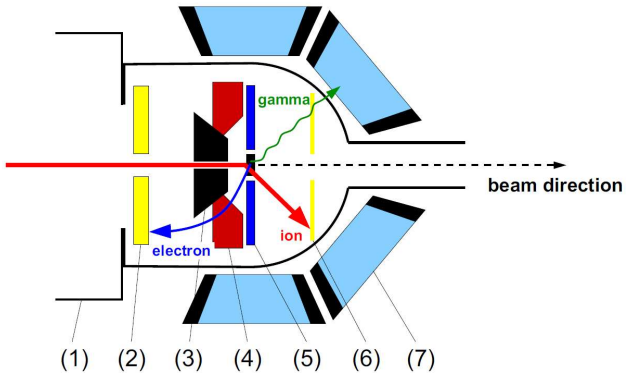


***Figure 2.4:*** *Cross section schematic of the SPICE spectrometer with individual components highlighted: (1) vacuum vessel, (2) Silicon detector for ICEs, (3) photon shield, (4) magnetic lens, (5) target housing, (6) Silicon ion detector and (7) HPGe detectors of TIGRESS. [13]*

## 2.5 Two-Stage Magnet Spectrometers

The University of Warsaw houses an ICE spectrometer that used two techniques of magnetic lensing for "in-beam" spectroscopy within the OSIRIS-II $\gamma$-ray array. A two-stage magnetic lens combines a "collector" magnet lens and a "transport" magnet lens. Four permanent plates (Nd-Fe-B material) are placed radially near to the target and guide the electrons away from the target (using a perpendicular magnetic field) and towards the detector, hence "collecting" the electrons. Positrons and other $\delta$-particles are also suppressed in the collector. A parallel magnetic field, created by 4 Nd-Fe-B

rings, are used to "transport" the electrons to the detector array. The overall distance from target to detector is also therefore large, reducing background further. There is a low amount of material within the target chamber (only the collector magnets) so low background from scattered radiation. This design also has a wide range of energy acceptance. When the original published design is compared to other devices it has a relatively low efficiency (peak of 0.4% at 300 keV) [14]. However, since this publication some improvements have been made, a efficiency that is now comparable to other designs has been published (5% at 500 keV) [15].

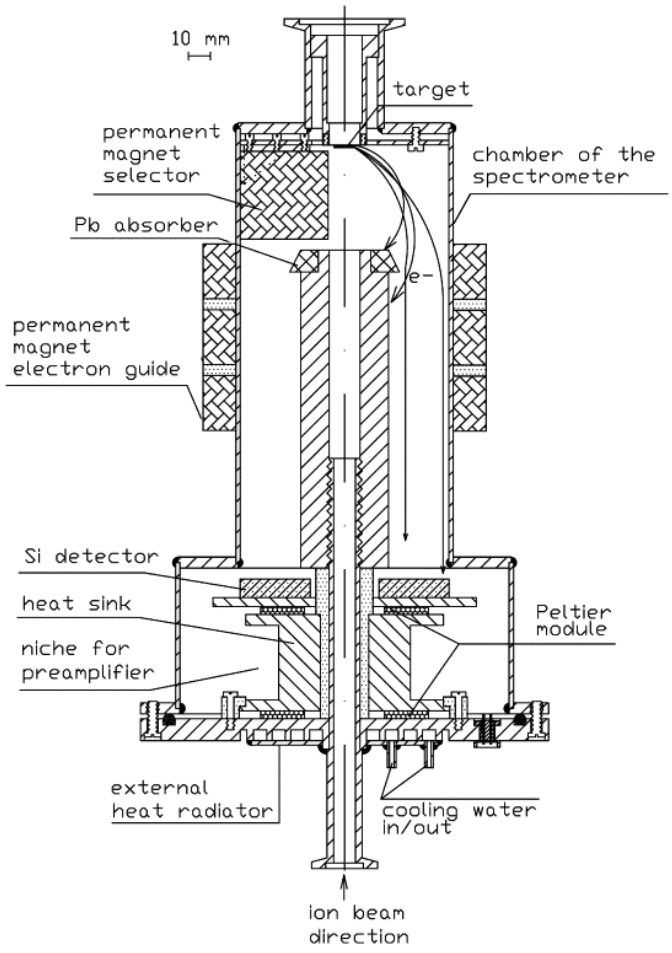


***Figure 2.5:*** *Schematic of the two stage electron spectrometer for the OSIRIS-II array. Figure shows the paths of electrons through both stages of magnetic lensing. [14]*

# Chapter 3

# Theory

## 3.1 Nuclear Decay

Nuclei will decay in order to acquire a more stable configuration. When a nucleus is unstable it will decay primarily by emitting $\alpha$-particles or $\beta$-particles, each decay taking the nucleus closer towards the valley of stability. It is common for a nucleus that has undergone a decay, as before mentioned, to be left in a state with some excitation energy. These states then decay through the emission of $\gamma$ rays, Internal Conversion Electrons (ICE's) or an electron/positron pair (via Internal Pair Formation). Some excited states can beta decay or proton decay, however this is less common.

### 3.1.1 Beta Decay

$\beta$-decay occurs mostly in neutron or proton rich nuclei, away from the valley of stability. This happens through the following processes [16]:

- Negative Beta Decay, $\beta^-$, a proton converts into a neutron emitting a positron and an electron neutrino.

$$p \rightarrow n + e^+ + \nu_e$$

- Positive Beta Decay, $\beta^+$, a neutron converts into a proton emitting an electron and an anti-electron neutrino.

$$n \rightarrow p + e^- + \bar{\nu_e}$$

- Electron Capture, the electron wavefunction overlaps with the nuclear wavefunction allowing an electromagnetic interaction with one of the protons. This forms a neutron and an electron neutrino.

$$p + e^{-} \rightarrow n + \bar{\nu_e}$$

In the first two processes there is an emission of two particles. The energy spectra of these two particles form a continuous distribution form 0 to Q (the mass difference between transitioned states). From electron capture we see distinct x-ray peaks where electrons move to fill the valence space left by the captured electron. If the resulting nucleus is left with an excitation energy that is larger than a given particle separation threshold energy, then a nucleon or an $\alpha$-particle may be emitted as the state decays. These are known as $\beta$ delayed emissions [17].

The alignment of the emitted electron and neutrino's spins determine the energy state that the nucleus can decay into. Allowed Fermi decay occurs when the particles have anti-parallel spins ($S$=0) and the net change in angular momentum through the decay is $\Delta I$=0, this is seen in "pure" form when the initial and final nuclear spins are both equal to 0 (i.e. a decay of $0^+ \rightarrow 0^+$). Allowed Gamow-Teller decay, when the particles have parallel spins ($S$=1), allows an angular momentum of unit 1 to be carried away by the emitted particles, i.e. $\Delta I$=0,1. For the allowed decays the particles are not allowed to carry orbital angular momentum ($l$=0), therefore a beta decay with $\Delta I$=0,1 with no change in parity is the most likely form of decay. It is also possible for there to be a mixing of these two decay forms. This is seen when both selection rules are satisfied, $\Delta I$=0 but the initial and final nuclear spins are not equal to 0.

A nucleus can also go through an order of forbidden beta decay, with the order of forbiddenness dependent on the value of orbital angular momentum that the emitted particles carried away. The higher the order, the lower the probability of the decay. Similar to allowed decays, forbidden decays come as Fermi or Gamow-Teller decays depending on the alignment of the emitted particles spins. For the first-forbidden decay the spins ($S$=0 for Fermi or $S$=1 for Gamow-Teller) are coupled to an orbital angular momentum of $l$=1, this gives a $\Delta I$=0,1 or a $\Delta I$=0,1 or 2 respectively. This decay also gives rise to a change in the parity, $\Delta\pi$=yes. This pattern is repeated for all following odd orders of forbidden decays with the respective unit of orbital angular momentum carried away. For second-forbidden decays the spins are couple to the orbital angular

momentum carried away of $l$=2 and this gives rise to a $\Delta I$=2,3 and no change in parity. This is then repeated through all following even orders of forbiddenness with a respective change in orbital angular momentum [18] . A summary of this is shown in the table below .

***Table 3.1:*** *Summary of $\beta$ decay selection rules*

| Order of Forbiddenness | Angular Momentum Change, $\Delta I$ | Change in Parity, $\Delta\pi$ |
|---|---|---|
| Allowed Decay | 0, 1 | no |
| 1st | 0, 1, 2 | yes |
| 2nd | 1, 2 | no |
| 3rd | 2, 3 | yes |
| 4th | 3, 4 | no |

### 3.1.2 Decay of Nuclear Excitation

#### Channels of Decay

A nucleus left in an excited state, after particle emission or a nuclear reaction, has a number of alternative decay modes:

- $\gamma$-ray emission, is the process of a nucleus releasing excitation energy through the emission of electromagnetic radiation. The energy of the photon emitted is equal to the energy difference between transitioned states.

- Internal Conversion Electrons, due to overlaps in the spatial wave functions of the nucleus and its orbiting electrons, it is possible for a transfer of excitation energy to an electron. This electron is then ejected from the atom with an energy equal to the energy of the transition less the binding energy of the electron [19].

- Internal Pair Formation, it is also possible for the energy to be released with the emission of an electron/positron pair. This has a minimum energy of 1.022 MeV, the energy needed to create the mass of the particles [20].

- Higher order decay modes, these includes processes such as two-photon decay [21]. These are orders of magnitude weaker transitions than the before mentioned and so will not be discussed further.

### Multipolarity

When the nucleus is left in an excited state it has a probability of decaying to the ground state or a lower energy state. The transition between these states causes a re-distribution of charges or currents within the nucleus, where there are variations in these re-distributions, a radiation field can be observed. This radiation field is dependent on the multipolarity of the transition. The multipolarity is labelled with two parts and comes in the form of "$\pi L$". In this form $\pi$ defines the mode/cause of the transition. If the transition is due to a current re-distribution it is an electric transition and so labelled "$E$". If the transition is due to a charge redistribution then it is a magnetic transition and is labelled "$M$". The second part of this labelling is dependent on the maximum angular momentum that is carried away from the nucleus in the transition, i.e. "1" means a maximum of 1 unit of angular momentum can be taken away by the radiation field. This also refers to the multipole order of the transition, for instance a "1" would suggest a dipole transition while a "0" would suggest a monopole transition. For example there is no "*M0*" transition because magnetic monopoles do not exist, however we can observe "*E0*" transitions [22].

In order to determine the multipolarity of a given transition then some information is needed about the initial and the final state. If we can observe the radiation (from one of the before described processes) and perform angular correlation measurements on these fields then we can determine the initial and final states from which the radiation originated. If the angular momentum and the parity of both states are known then the multipolarity can be deduced. Shown in the table below are the dominant nuclear transitions [23].

Of particular note is the "*E0*" transition. This occurs between $J^+ \rightarrow J^+$ states and because there is no change in angular momentum, a $\gamma$-ray emission is forbidden. This means that only ICE and IPF emissions (and other second order processes) are allowed through this transition.

***Table 3.2:*** *Dominant multipole orders for nuclear transitions*

| Multipolarity of Transition | Maximum Angular Momentum Change | Change in Parity |
|---|---|---|
| *E0* | 0 | no |
| *E1* | 1 | yes |
| *M1* | 1 | no |
| *E2* | 2 | no |
| *M2* | 2 | yes |
| *E3* | 3 | yes |
| *M3* | 3 | no |
| *E4* | 4 | no |
| *M4* | 4 | yes |

The transition between states is not necessarily described by a singular multipolarity but through a mixture of multipolarities. The multipolarity mixing ratio, $\delta$ ($\pi L$ field) is the ratio of two absolute transition amplitudes in terms of their photon emission:

$$\delta(\frac{\pi' L'}{\pi L}) = \frac{\gamma(\pi' L')}{\gamma(\pi L)} \tag{3.1}$$

**Conversion Coefficients**

Every state will have a probability of decaying, described by the decay constant of the parent state, $\lambda_T$. The decay constant is equal to the sum of all the partial decay constants for the relevant state, these describe the probability of a state decaying to a particular state. We can write the decay constant of the parent state as:

$$\lambda_T = \lambda_1 + \lambda_2 + ... + \lambda_N \tag{3.2}$$

We can also describe the probability of a transition between specific states decaying through a particular process, in a similar way as mentioned above. Defining the probability of a state decaying by the release of a gamma-ray as, $\lambda_\gamma$. We can relate this to the probability of an ICE emission using the internal conversion coefficient, $\alpha_e$:

$$\alpha_{ICE} = \frac{\lambda_e}{\lambda_\gamma} \tag{3.3}$$

Where $\lambda_e$ and $\lambda_\gamma$ are the decay constant for ICE emission and gamma-ray emission respectively.

It is customary to describe the conversion coefficients in terms of the atomic subshells (e.g. $\alpha_{L1}$, $\alpha_{L2}$, etc.) or in terms of the major atomic shells (e.g. $\alpha_K$, $\alpha_L$, etc.). We can use a similar concept to describe the probability of an IPF emission, $\alpha_\pi$:

$$\alpha_{IPF} = \frac{\lambda_\pi}{\lambda_\gamma} \tag{3.4}$$

Where $\lambda_\pi$ and $\lambda_\gamma$ are the decay constant for IPF emission and gamma-ray emission respectively.

It can be seen that for the before mentioned "*E0*" transition that no associated conversion coefficient can be described due to the lack of photon emission. The principle of conversion coefficients can be used in the case of mixed multipolarity transitions, following from equation 3.1:

$$\alpha = \frac{\alpha(\pi L) + \delta^2 \alpha(\pi' L')}{1 + \delta^2} \tag{3.5}$$

Where $\alpha(\pi L)$ and $\alpha(\pi' L')$ are the conversion coefficients for the pure multipolarity components.

**Quadrupole Moment**

Protons within the nucleus and electrons orbiting the nucleus together create an electric dipole moment within the atom. Depending on the shape of the nucleus, it is possible for there to be two identical but displaced dipole moments, i.e. an electric quadrupole moment. This can be shown by the following:

$$Q = \frac{1}{e}(3z^2 - r^2)\rho d\tau \tag{3.6}$$

where e is the charge of an electron, z is the distance from the nucleus centre to nucleus edge, r is the average radius of the nucleus and $\rho d\tau$ is the charge density within a volume. If z=r the nucleus is perfectly spherical and Q=0, therefore there

is no quadrupole moment. When z>r, Q=+ve and the nucleus has a quadrupole moment and is of a prolate shape. Conversely when z<r, Q=-ve the nucleus again has a quadrupole moment but the nucleus is of an oblate shape [22] and [24].

## 3.2 *E0* transitions

Electric monopole transitions can only proceed through ICE or IPF, with single photon emission forbidden by angular momentum conservation. This means the transition probability from equation 3.2 can be reduced to:

$$\lambda(E0) = \frac{1}{\tau(E0)} = \lambda_e(E0) + \lambda_\pi(E0) = \rho^2(E0) \times [\Omega_e(E0) + \Omega_\pi(E0)] \tag{3.7}$$

where $\tau(E0)$ is the partial mean lifetime for the $E0$ decay from the initial state. $\lambda_e(E0)$ and $\lambda_\pi(E0)$ are the transition probabilities for ICE and IPF respectively. The quantities $\Omega_e(E0)$ and $\Omega_\pi(E0)$ are the electronic factors for ICE and IPF respectively [25], these are calculated from atomic number, transition energy and atomic electron shell involved. $\rho(E0)$ is known as the dimensionless monopole transition strength. Within this is all of the related information about nuclear structure, in the form of the monopole matrix element $M(E0)$:

$$\rho(E0) = \frac{\langle f|M(E0)|i\rangle}{eR^2} \tag{3.8}$$

where $e$ is the electronic charge, $R = r_0 A^{1/3}$ nuclear radius, $A$ is the atomic mass number and $r_0$=1.20 fm [26].

There are many experimental methods of determining the value of this $\rho(E0)$ value, these are dependent on the observables measurable in a given experiment. For instance if the partial mean lifetime of the $E0$ transition can be determined then:

$$\rho^2(E0) = \frac{1}{[\Omega_e(E0) + \Omega_\pi(E0)] \times \tau(E0)} \tag{3.9}$$

Or in the case where if there is an observable arbitrary transition of $E2$ to the final state in question, $\rho(E0)$ can be obtained from the expression:

$$\rho^2(E0) = q_K^2(E0/E2) \times \frac{\alpha_K(E2)}{\Omega_K(E0)} \times \lambda_\gamma(E2) \tag{3.10}$$

where $q_K^2(E0/E2) = I_K(E0)/I_K(E2)$ (i.e. the relative intensities of the $E0$ and $E2$ K-conversion components respectively [27]). The quantity $\Omega_K(E0)$ is the electronic factor for the K component of the $E0$ pure multipolarity contribution. The quantities $\alpha_K(E2)$ and $\lambda_\gamma(E2)$ are the conversion coefficients and $\gamma$ transition rate of the $E2$ pure multipolarity contribution [28].

## 3.3 Electron Interactions with Matter

Electrons interact with matter via coulomb scattering with atomic electrons. Through this process an electron will follow an erratic path due to the large deflections in these collisions. A random walk is taken through a material, meaning the thickness of the material is very different to the path taken. A straight on collision with another electron is also hard to distinguish in this situation as a large quantity of the initial energy can be passed to the struck electron, with no way to tell apart the two electrons. Another feature of these interactions is Bremsstrahlung radiation, the emission of electromagnetic radiation due to the large acceleration that is experienced by the electron as it is deflected by another electron [29]. This means that the energy lost by a unit of path length taken by the electron is shared by two components: the loss through radiation and the loss through collisions.

$$\frac{dE}{dx} = (\frac{dE}{dx})_c + (\frac{dE}{dx})_r \tag{3.11}$$

Where the subscripts c and r stand for collisional losses and the radiation losses respectively, $x$ is the unit of path length and $E$ is the energy. These can be described relative to each other as:

$$\frac{(dE/dx)_r}{(dE/dx)_c} \approx \frac{T + mc^2}{mc^2}\frac{Z}{1600} \tag{3.12}$$

Where T is the kinetic energy of the electron and Z is the effective charge of the material. This is hard to integrate in order to calculate the actual range of electrons in a material due to the random nature of the electron path. However, this range can be measured empirically and so this data is used in order to create a range-energy relationship [18]. An example of this relationship with air and aluminium can be seen in Fig. 3.1.

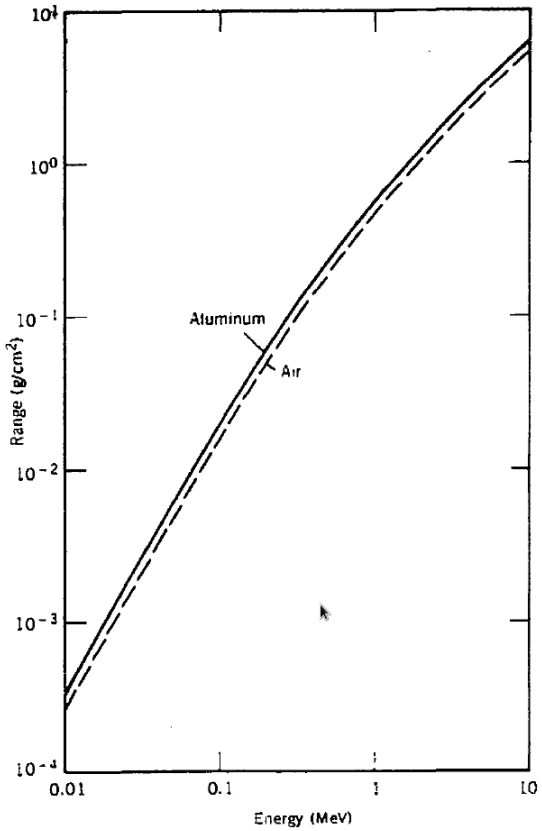


***Figure 3.1:*** *Empirical Range-energy relationship for electrons in air and in aluminium. Taken from Introductory Nuclear Physics by Kenneth S. Krane [18]*

## 3.4 Gamma-Ray Interactions with Matter

How a $\gamma$-ray interacts with a material that it is travelling within is important in understanding the background that will be seen within the detector. A $\gamma$-ray has three main processes of interacting inside a material, which are dependent on the energy of the photon. These are photoelectric absorption, compton scattering and pair production. Fig. 3.2 shows the energy ranges over which these processes are dominant [18].

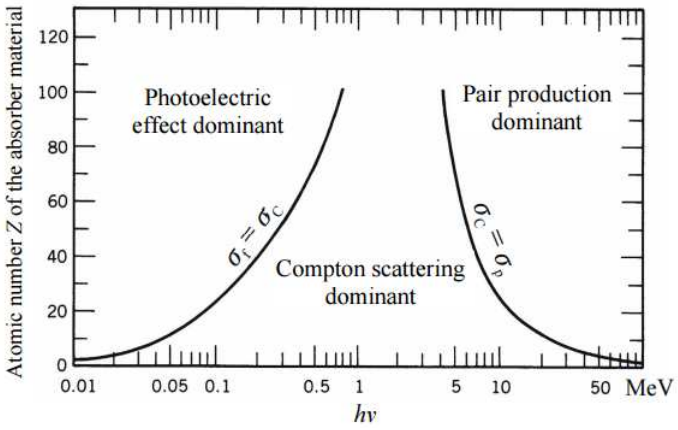


***Figure 3.2:*** *The three $\gamma$-ray interactions with matter and their regions of dominance. Taken from Introductory Nuclear Physics by Kenneth S. Krane [18]*

### 3.4.1 Photoelectric Absorption

This process occurs at low energy (<100 keV) $\gamma$ rays predominately. The photon is absorbed by an atomic orbital electron, ejecting it from the atom. The kinetic energy of the released electron is then the energy of the photon less the binding energy of the electron orbit [30]:

$$E_{e^-} = E_\gamma - B_e \tag{3.13}$$

The probability of such an event is hard to calculate precisely but it is known to be proportional to $Z^4$ and inversely proportional $E_\gamma^3$ with a discontinuity in probability around the binding energies of the electron orbitals [31]. It is given a linear absorption coefficient, $\tau$, which is calculated from the photoelectric cross section like so:

$$\tau = 0.033^* \sigma_{cs} \tag{3.14}$$

Where $\sigma_{cs}$ is the cross section of the interaction. After emission, the valence space is then filled by electron re-arrangement with the emission of an X-ray or Auger electron.

### 3.4.2 Compton Scattering

Compton scattering is the process of a $\gamma$-ray scattering off of a free or nearly free electron. This process leaves a scattered electron (with some of the photon energy) and

a less energetic $\gamma$-ray. Approximating the electron as free and at rest, we can determine the initial energy of the photon using the Compton-scattering formula:

$$E_{\gamma}^{'} = \frac{E_{\gamma}}{1 + (E_{\gamma}/mc^2)(1 - cos\theta)} \tag{3.15}$$

By integrating over all angles of the Klein-Nishina formula we can calculate a cross section for the absorption of photons through the compton scattering process. This is given by:

$$\sigma_c = \frac{\pi r_0^2}{\alpha}\Big(\Big[1 - \frac{2(\alpha+1)}{\alpha^2}\Big] ln(2\alpha+1) + \frac{1}{2} + \frac{4}{\alpha} - \frac{1}{2(2\alpha+1)^2}\Big) \tag{3.16}$$

Where, $\alpha$ is the photon energy in units of electron rest energy ($\alpha = E_{\gamma}/mc^2$) and $r_0$ is the classical electron radius ($r_0 = e^2/4\pi\epsilon_0 mc^2$). This cross section can be related to the linear Compton absorption coefficient, $\sigma$, by the following relationship:

$$\sigma = \sigma_c NZ \tag{3.17}$$

### 3.4.3 Pair Production

This is where a photon spontaneously creates an electron-positron pair. This process has a minimum threshold energy of 1.022 MeV which is the equivalent of the rest mass-energy needed to create the particle pair. It is dominant over the other two processes after 5 MeV [32]. The energy distribution of this process is:

$$E_{\gamma} = m_{e^+}c^2 + T_{e^+} + m_{e^-}c^2 + T_{e^-} \tag{3.18}$$

The probability of this process is given by the term, $\kappa$ and is the summed probability of the process occurring in the field of an electron, $\kappa_e$, and the probability in the field of a nucleus, $\kappa_n$.

### 3.4.4 Gamma-Ray Attenuation Co-efficient

As $\gamma$ rays pass through a material, the intensity follows an exponential attenuation with a distance through a material of $x$. The relationship is given as:

$$I = I_0 e^{-\mu x} \tag{3.19}$$

Where $I_0$ is the initial intensity of the $\gamma$-ray. The term $\mu$ is known as the linear attenuation coefficient of the material, it is dependent on the effective charge of the nuclei within the material, $Z_{eff}$, as well as the density of the material, $\rho$, and the energy of the incoming $\gamma$-ray [33]. The coefficient is the sum of the probabilities of photoelectric absorption, $\tau$, compton scattering, $\sigma$, and pair production, $\kappa$ [34].

## 3.5 Magnetostatics

As electrons orbit an atom, they create a current. This produces a magnetic dipole moment which can be defined as:

$$m = \frac{e}{2m_e} l \tag{3.20}$$

where $e$ is the charge of an electron, $m_e$ is the mass of the electron and $l$ is the angular momentum of the respective electron [35]. To find the magnetisation of a material, M, we have to integrate the magnetic dipole moments over the volume of the material, $M = n\mathbf{m}$ . Therefore a material with no magnetisation has no net magnetic dipole moment. A magnetised material can be created by aligning these individual magnetic dipole moments.

The magnetisation value can be related to the BH energy product of the material by the following:

$$M = \frac{B}{\mu_0} - H \tag{3.21}$$

Where B is the magnetic flux density, H is the magnetic field intensity and $\mu_0$ is the permeability of free space [36].

# Chapter 4

# CEDAR

CEDAR is designed to be an upgraded internal conversion electron spectrometer to the one that is in used currently with the GRIFFIN array. The PACES array (Pentagonal Array for Conversion Electron Spectroscopy) was originally designed for the $8\pi$ array, it was discussed further previously in section 2.3. As an upgrade CEDAR has a number of criteria to fulfill:

- The efficiency of CEDAR should be higher than PACES over a selected energy range. PACES has an efficiency of $\sim$5% across all energy, further discussed later.
- PACES had a limited count rate due to the limited number of detection segments in the array. Therefore an improved count rate in CEDAR is required.
- All sources of background should be reduced as much as possible.
- The effect of CEDAR on GRIFFIN should be as limited as possible, further discussed later.
- The effect of CEDAR on SCEPTAR should be as limited as possible, further discussed later.

The count rate of CEDAR will be improved by increasing the segmentation of the Silicon Lithium detectors inside the array. As such, four trapezoidal lithium drifted silicon (Si(Li)) detectors will be used, each will be segmented further. Each detector has an active area of 1307.25 $mm^2$ for a combined total of 5229 $mm^2$ within the array. This is then segmented into 12 segments per detector, totalling 48 segments over the entire array meaning an increase in the count rate ratio of CEDAR over PACES almost

10 fold. A large benefit of having 4 detectors within CEDAR is in the case of a failure or detector breakage, which can have a long repair lead time, CEDAR can still be operational. The lower cost of these smaller detectors could provide the opportunity to possibly purchase spares. Meaning that CEDAR can be ran at full capacity for all proposed experiments.

In order to avoid hampering the efficiency of the upstream lampshade of the GRIFFIN array the detectors had to be placed so that they did not cover any of the solid angle occupied by this lampshade. Due to the geometry of GRIFFIN this gave a square based pyramidal cone, rotated around the beam axis by 45 degrees and with a base angle of 22.5 degrees. This gives rise to the shape and design as shown in Figure 4.2. The detectors are placed with an offset to the "beam axis" by and angle of 22.5 degrees. The size of detector could be maximized by rotating the detectors around the beam axis 45 degrees, similar to the lampshade HPGe's of GRIFFIN. However, the angle displayed is preferable relative to the position of the individual magnets of the magnetic lens.

There are many forms of background that would be seen within CEDAR, the design takes this into account and reduces them in the following ways:

- Photons: After nuclear decay many $\gamma$ rays are emitted, causing a significant background. In order to prevent this a photon shield of high density, high Z material has been designed to sit in between the mylar tape of GRIFFIN and the detectors. This shield has been designed to attenuate 99.9% of 511 keV $\gamma$ rays and will be further discussed in section 5.1.

- $\beta^+$ decay: A positron emitted from a $\beta^+$ decay will be rejected by the magnetic lens. This is due to having an opposite charge in comparison to an electron and so being bent away from the detectors.

- $\beta^-$ decay: It is very difficult to tell an internal conversion electron and a $\beta^-$ particle apart. However, by using a temporal coincidence with the SCEPTAR array the peak to background that is caused by $\beta$ decay can be reduced at cost of some statistics.

Figure 4.1 below displays an example of a simulated magnetic field created using a lens of 8 magnets. A slice is plotted at 22.5 away from the center of the magnet lens,

-30 mm in Z (upstream from the source) and a magnetisation value of 900,000 A/m. This slice is at an angle halfway between a magnet pairing and the symmetry in the x-y plane along this axis of the magnetic field can be seen within this figure. As the ideal magnetic field shape for the electron bending is circular in the x-y plane, this achieved within the simulation.

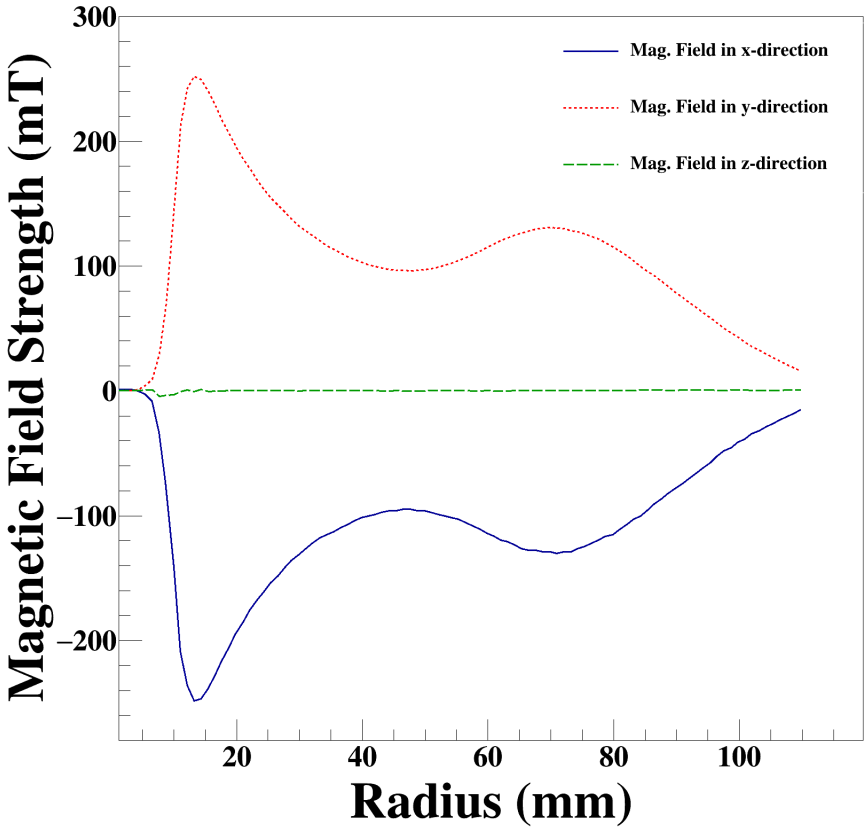


***Figure 4.1:*** *Example magnetic field of a sample lens, as a function of radius in a slice of 22.5 away from the center of a magnet. The data was collected at -30.0mm in Z (upstream from the source).*

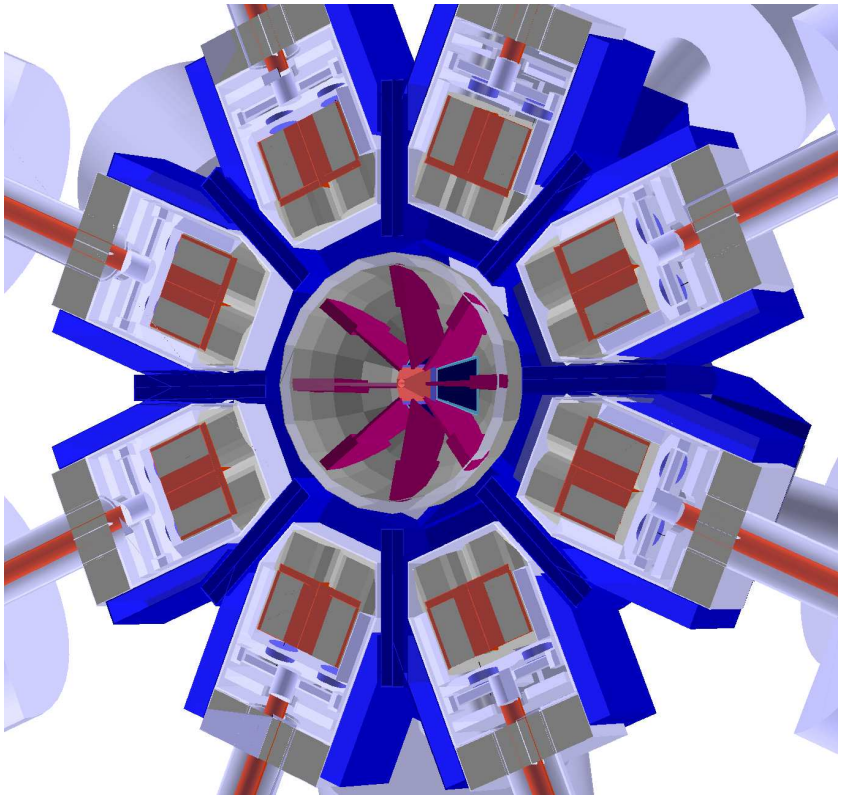

***Figure 4.2:*** *A side view of CEDAR within GRIFFIN, as seen from the downstream angle. This highlights how all of the various components fit together. Of note, this angle shows how all of the magnets are placed within the "shadow" zone of the GRIFFIN BGO's (shown in blue)*

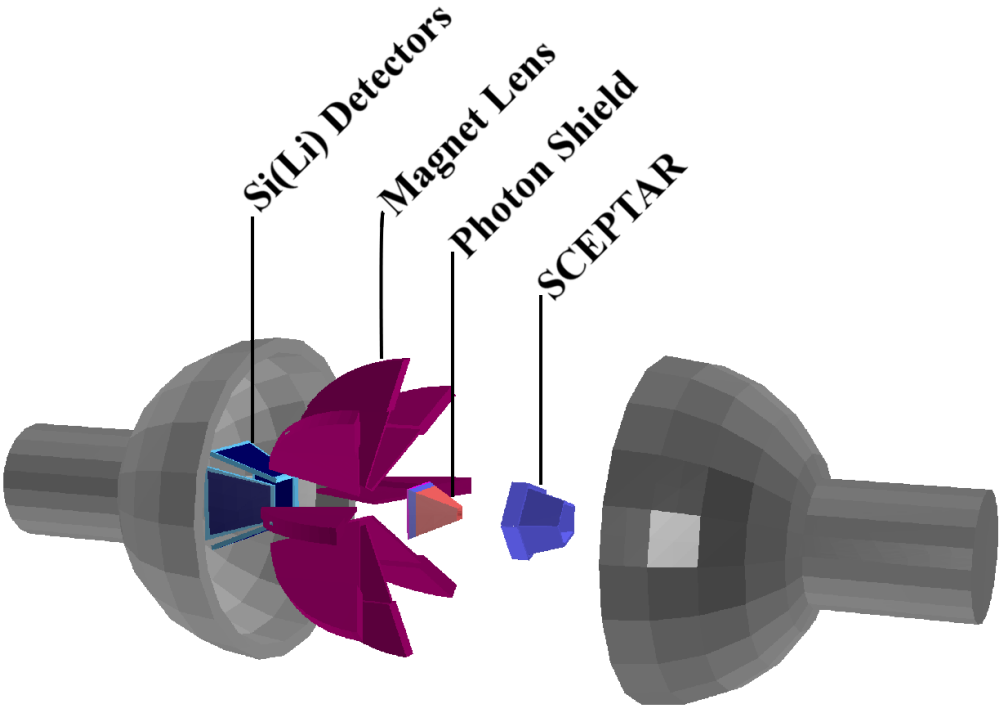


***Figure 4.3:*** *The CEDAR and SCEPTAR set up in an exploded view. Highlighting the shape of the various components: Si(Li) detectors, Magnets, Photon Shield and plastic paddles of SCEPTAR.*

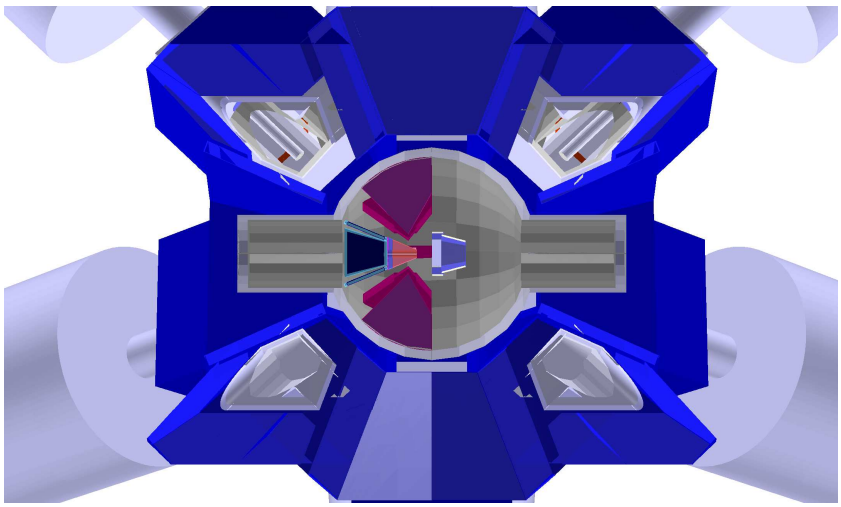

***Figure 4.4:*** *A side view of GRIFFIN with both SCEPTAR and CEDAR. This view shows how the Si(Li) detectors of CEDAR are placed within the "shadow zone" of the upstream BGO's of GRIFFIN.*

# Chapter 5

# Simulations and Results

By using the Geant4 (a monte-carlo simulation package [37]) and COMSOL software, iterations of the spectrometer design have been created. COMSOL is a finite element analysis multiphysics platform used in order to produce a magnetic field table [38]. COMSOL breaks a 3 dimensional object into a "mesh" of finite tetrahedrons, these mesh elements are then used in order to solve PDE's for an unknown number of degrees of freedom. For the case of the permanent magnet the 3-D geometry mesh elements are treated as small electromagnets, all of which contribute towards the overall magnetic field. By defining the geometry's magnetization value, M, the complete magnetic field for a defined volume space or "world" can be solved for [39].

The principle of monte-carlo states that for $S$ successes from $N$ trials the value of $S/N$ gives a good approximation for the expected value from an experiment. Through the use of digitalized computers one can solve complex problems from simple techniques [40]. Geant4 is a software package used to simulate the emission and motion of various particles within defined a geometry, essentially a monte-carlo framework for physical problems. Importing the magnetic table into Geant4, which then interpolates the field between data points, a simulation can be run. The data from these simulations is then exported into the analysis software ROOT, results are analyzed in order to to determine the effectiveness of the design [41]. Via this three step process the design of CEDAR was done to minimize background and maximize efficiency.

## 5.1 Photon Background Suppression

$\gamma$ rays are a large source of radiation after the decay of unstable isotopes. For electron spectroscopy this produces a large source of background if not dealt with within the array. As previously discussed, previous electron spectrometers employ a photon shield between the source and detector in order to absorb or scatter the $\gamma$ rays.

The effectiveness of a photon shield can be calibrated to a given chosen energy value. This is due to the energy dependence of the linear attenuation coefficient of a given material. The chosen energy value for this design was 511 keV, this is a useful value as it is the energy of the $\gamma$ rays produced in a electron-positron annihilation. As GRIFFIN and SCEPTAR are used in decay studies, which include $\beta^+$ decays, this is a suitable value.

As you can see from figure 5.1 the linear attenuation coefficients can be used to calculate the depth of given materials needed to attenuate (scatter/absorb) a selected percentage of $\gamma$ rays. From this it can be seen that for 99.9% attenuation: 30 mm of Pb, 25 mm of W and only 20 mm of Pt, Ir or Os. The cost of a Pt, Ir or Os photon shield makes them unrealistic candidates and W is very difficult to machine. Therefore, an alloy of 97.5% Ta and 2.5% W was chosen for the photon shield material.

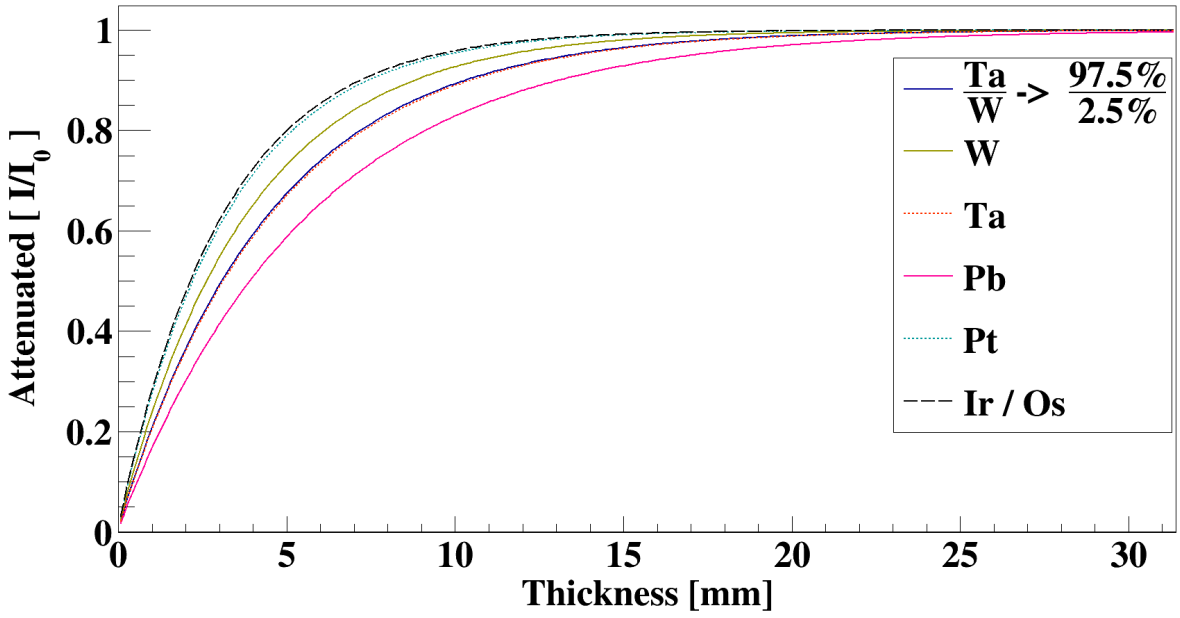


***Figure 5.1:*** *A plot showing the attenuation of 511 keV $\gamma$ rays for varying materials.*

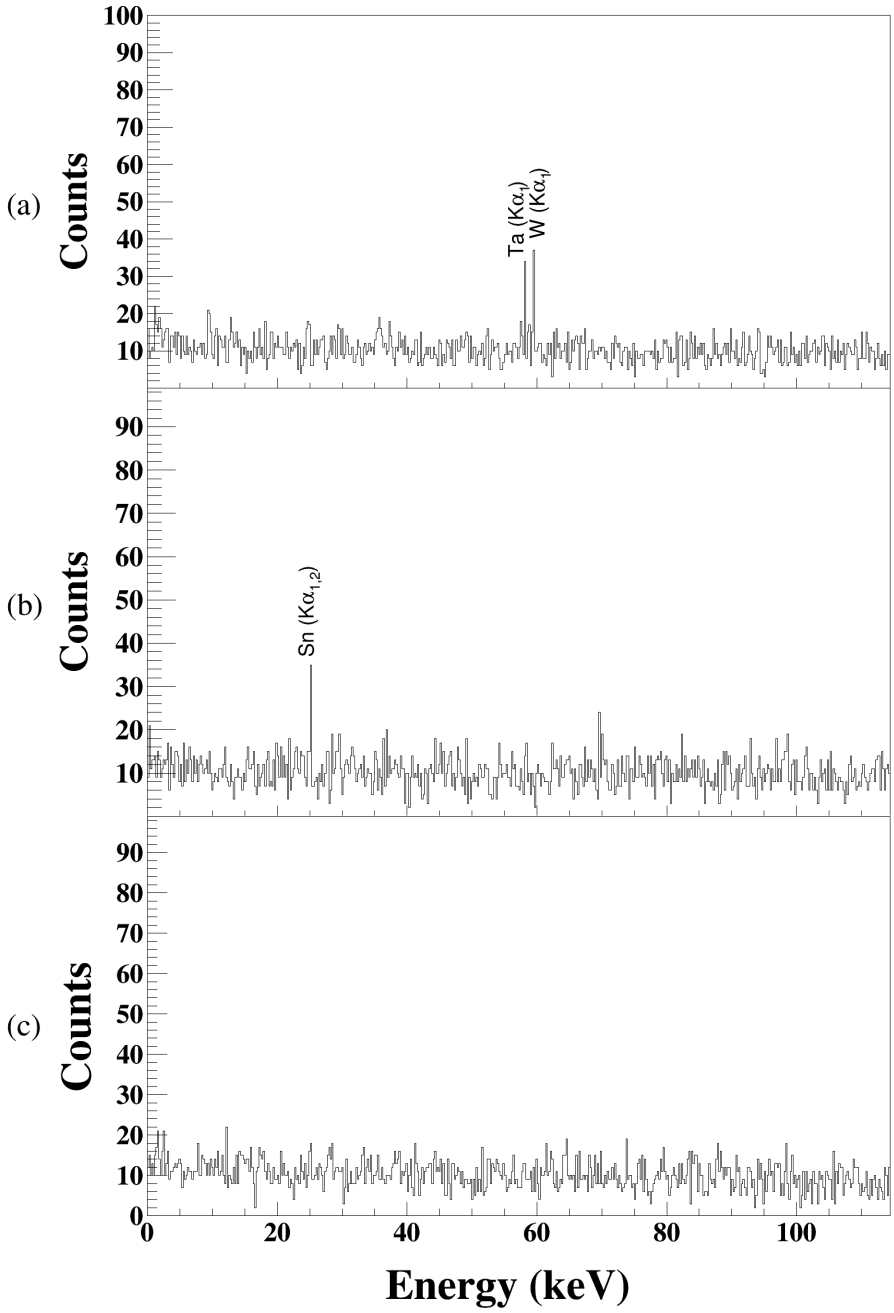


***Figure 5.2:*** *Simulated low energy spectra of 30 million 2 MeV $\gamma$ rays passing through (a) the 25 mm Ta/W alloy, (b) the Ta/W allow and Sn later and (c) all three layers of the photon shield.*

However, by reducing the background from these $\gamma$ rays another source of background is introduced into the array. The photon shield can be ionized by incident $\gamma$ rays and other particles. This in turn produces X-ray florescence and PIXE (Particle Induced X-ray Emission) as the ionized Ta/W allow atomically de-excites. The X rays

can be attenuated in a similar manner to the incident $\gamma$ rays. (Also, as the energy of emitted X rays is proportional to the Z of the material, by reducing the material Z the energy of subsequently emitted X rays can be reduced. Therefore, it was calculated that for the $\sim$58 keV X rays from the Ta/W alloy a 4 mm layer of Sn was needed. Following this a 0.1 mm layer of Cu would be needed to scatter/absorb the 25 keV X rays from the Sn, for ease of manufacturing a 1 mm layer of Cu was used in the final design.

By using packages within Geant4 the simulation of the previously mentioned processes can be performed. Figure 5.2 shows the various detected X rays from each layer of photon shield. The top layer (composed of a Ta/W alloy) the X-ray peaks of 58 keV from Ta and 59 keV from W can be seen, displayed in Figure 5.2 (a). After the Sn layer is added these peaks are attenuated but now the 25 keV Sn X-ray can be detected, see Figure 5.2 (b). Lastly, employing the Cu layer now reduces the Sn X-ray peak, plus the 8 keV X-ray from the Cu is not observable above background level. The conclusion from all of this is that X rays are not of huge concern as a source of background. With the layout and size of the detectors behind the photon shield there is a natural suppression of X rays.

The effectiveness of this photon shield can be proven using the simulated decay of $^{207}$Bi under 4 cases, as shown in Figure 5.3 $^{207}$Bi decays mostly via the electron capture channel producing $^{207}$Pb fed into 4 excited states. These states then de-excite through the emission of $\gamma$ rays and ICEs, in this region of the nuclear chart the more likely decay is through ICEs. The emission of which will have an energy equal to the $\gamma$-ray energy minus the binding energy of the relevant atomic electron orbital. For simplicity the simulation only includes the emission of electrons from the K and L orbitals.

When there is no magnetic field or photon shield placed between the source and the detectors then the detection of internal conversion electrons and $\gamma$-rays is solely due to the solid angle coverage of the detectors and scatter from the chamber wall. This direct detection is the reason for the $\gamma$-ray peaks and respective compton edges. Also of note from Figure 5.3 (a) is the Auger electrons and X-rays emitted from the atomic de-excitation of $^{207}$Pb following the decay.

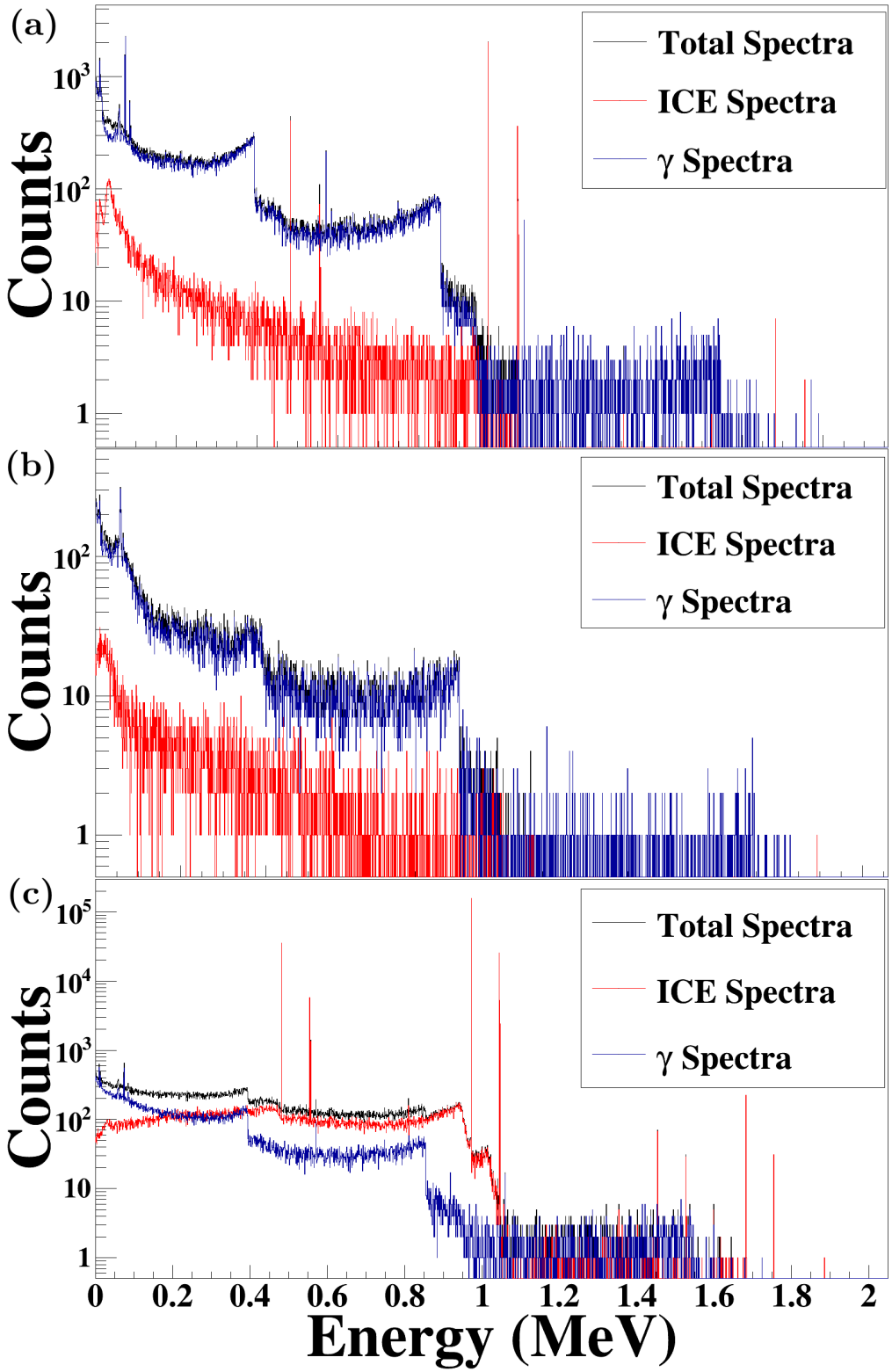


***Figure 5.3:*** *Simulated energy spectra of 20 million $^{207}Bi$ decays under three different cases. Each of the three showing the electron and $\gamma$ rays contribution to the total spectra: (a) when there is no photon shield or magnetic field present, (b) when the photon shield is in place but lacking a magnetic field to guide the electrons onto the detectors, and (c) when there is a photon shield and magnetic field in place.*

In placing the photon shield in between the source and the detectors the $\gamma$-ray and electron peaks are removed from the spectrum. With no clear line of sight for the $\gamma$ rays and electrons, the only detected particles are those that are scattered off the various components within the chamber and the chamber itself, as shown in Figure 5.3 (b). It can be seen that the counts across the entire energy range is dramatically reduced and a large proportion of the Auger electron and X-ray background is also removed.

Adding into the simulation the magnetic field causes a drastic change in the energy spectra observed, as seen in Figure 5.3 (c). The contribution to the spectra from $\gamma$ rays is unchanged from before adding in the magnetic field, however, the real difference is in the spectral contribution from the internal conversion electrons. It can be seen that the conversion electron spectra now contributes the majority of the total spectra observed.

## 5.2 Effect on GRIFFIN

A large limitation of the design of CEDAR is the planned combination of the detector with GRIFFIN, where CEDAR will be an ancillary device. As previously mentioned, CEDAR will make up the upstream hemisphere of the GRIFFIN target chamber and so it is important that CEDAR does not hamper the efficiency of GRIFFIN. GRIFFIN has two configurations for experimental usage, the first being a "high efficiency" configuration where the HPGe detectors that make up GRIFFIN are placed 110 cm away from the source (i.e. at the edge of the target chamber). This configuration has no suppression but a much higher efficiency for detection. The second configuration is a "high peak/total" configuration, in this setting the HPGe detectors are brought back to 145 cm away from the source allowing for sets of BGO's to placed around and in front of the HPGe detectors. This reduces the photopeak efficiency of the array but allows for suppression of the HPGEs, increasing the peak/total of GRIFFIN by removing random background coincidences.

When CEDAR is in use GRIFFIN will be used in the high peak/total configuration. This allows the permanent magnets within CEDAR to be designed such as they are within the 6.5° shadow zone of the GRIFFIN suppression shields. At this point it is useful to split GRIFFIN into 3 components: Upstream Lampshade, Corona and

Downstream Lampshade. The "Corona" is a set of 8 HPGe detectors all placed at 90° around the beam plane whist both lampshades make up 4 HPGe detectors placed at 45° and 135°. CEDAR therefore has been designed such that the 8 magnet positions are placed within the shadow zone of the corona suppression shields. It was not possible to do the same for the upstream lampshade HPGes due to a 22.5° rotational offset, thus the magnetic lens is placed within the solid angle of these HPGe detectors regardless of the final magnet design.

Using a magnet design of 8 magnets with a high angular thickness (∼8.8) an investigation into the effect of CEDAR on the efficiency of GRIFFIN was simulated. This magnet design exceeds the shadow zone of the GRIFFIN suppression shields for the corona of GRIFFIN. Figure 5.4 shows the results from that investigation. It can be seen that the downstream lampshade of GRIFFIN is uninhibited by CEDAR with none of the components of CEDAR actually lying within the downstream half of GRIFFIN. Figure 5.4 also shows that even though this particular design exceeds the shadow zone of the corona, the impact of this to the efficiency is minimal. This could be explained as only the most downstream corners of the magnet design edge into the detection zone of the HPGe detectors, meaning only a small amount of material is in direct line of sight of the HPGEs. This is also minimal as the magnetic lens only extends through half of the corona HPGes, as each HPGe has half of its detection zone upstream where the magnets are placed.

The largest impact seen within Figure 5.4 is within the upstream lampshade. As mentioned above the design of the magnets could not avoid the detection zone of both the corona and the upstream lampshade due to a 22.5° offset between the two. This is obvious in the loss of 3% peak efficiency and a smaller loss across the entire energy range. This is then reflected in the loss of a small amount of efficiency in the entire array and whilst disappointing this impact is relatively small, previous electron spectrometer designs required the removal of the entire lampshade for geometrical reasons. There is minimal impact on the peak/total of GRIFFIN due to the inclusion of CEDAR.

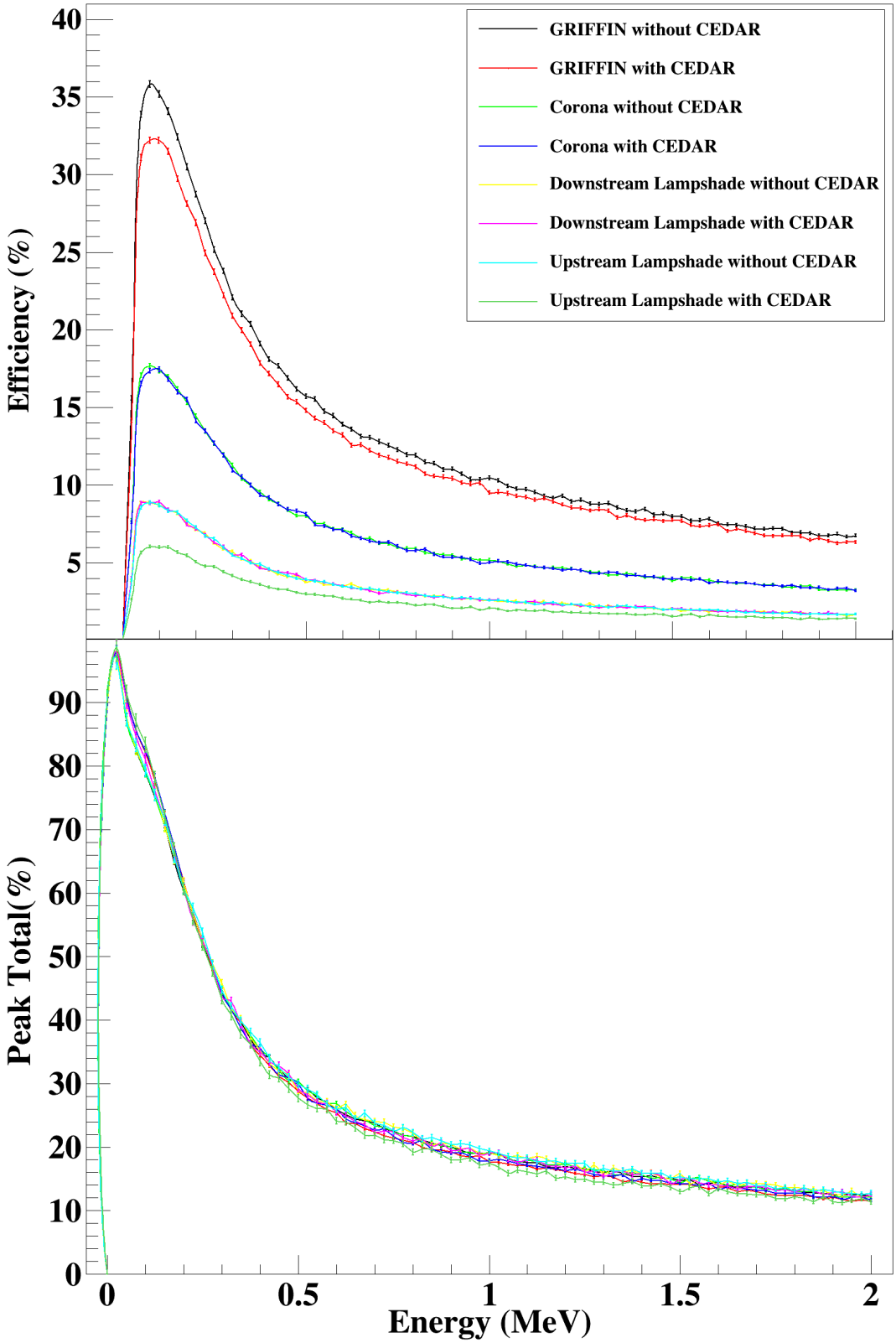


***Figure 5.4:*** *Effect of CEDAR on the Efficiency and Peak/Total of GRIFFIN and its three components: Upstream Lampshade, Corona and Downstream Lampshade*

## 5.3 Complex Sources

Figure - spectral comparison of PACES and CEDAR with Ba133, Co56 and Co60

The effectiveness of this design over the PACES array (which this design will replace) can be proven using a selection of simulated decays of other isotopes. Whilst $^{2}$07Bi is a very useful source within electron spectroscopy it is very highly converted for an isotope and so does not really show off the power of this design in full. For this 3 different isotope source decays have been chosen, as shown below:

- $^{6}$0Co - A very simple source decaying only to two different levels. It is very lowly converted.
- $^{5}$6Co - A more complex source with many different levels within the decay chain. Also lowly converted.
- $^{1}$33Ba - Similar to the $^{5}$6Co source but all of the transitions are of low energy (i.e. <500 keV).

$^{60}$Co decays mostly via the $\beta^+$ channel producing $^{56}$Fe fed into 2 excited states. These states then de-excite through the emission of $\gamma$ rays and ICEs, in this region of the nuclear chart the more likely decay is through $\gamma$ rays. For this isotope the main decay channels are at $\gamma$ ray energies of 1173 keV and 1332 keV. The atomic electrons are very weakly bound with the $e_K$ and $e_L$ binding energies equal to 8.33 keV and $\sim$1 keV. For simplicity the simulation only includes the emission of electrons from the K and L orbitals.

It can be seen within Figure 5.5 (a) that when using PACES it is very difficult to distinguish between the background, from $\gamma$ rays and scatter, and the electron peaks. However, when using the CEDAR array (Figure 5.5 (b)) the two K lines protrude clearly from the background and the L lines are closer in strength to the $\gamma$-ray lines that lies beside them.

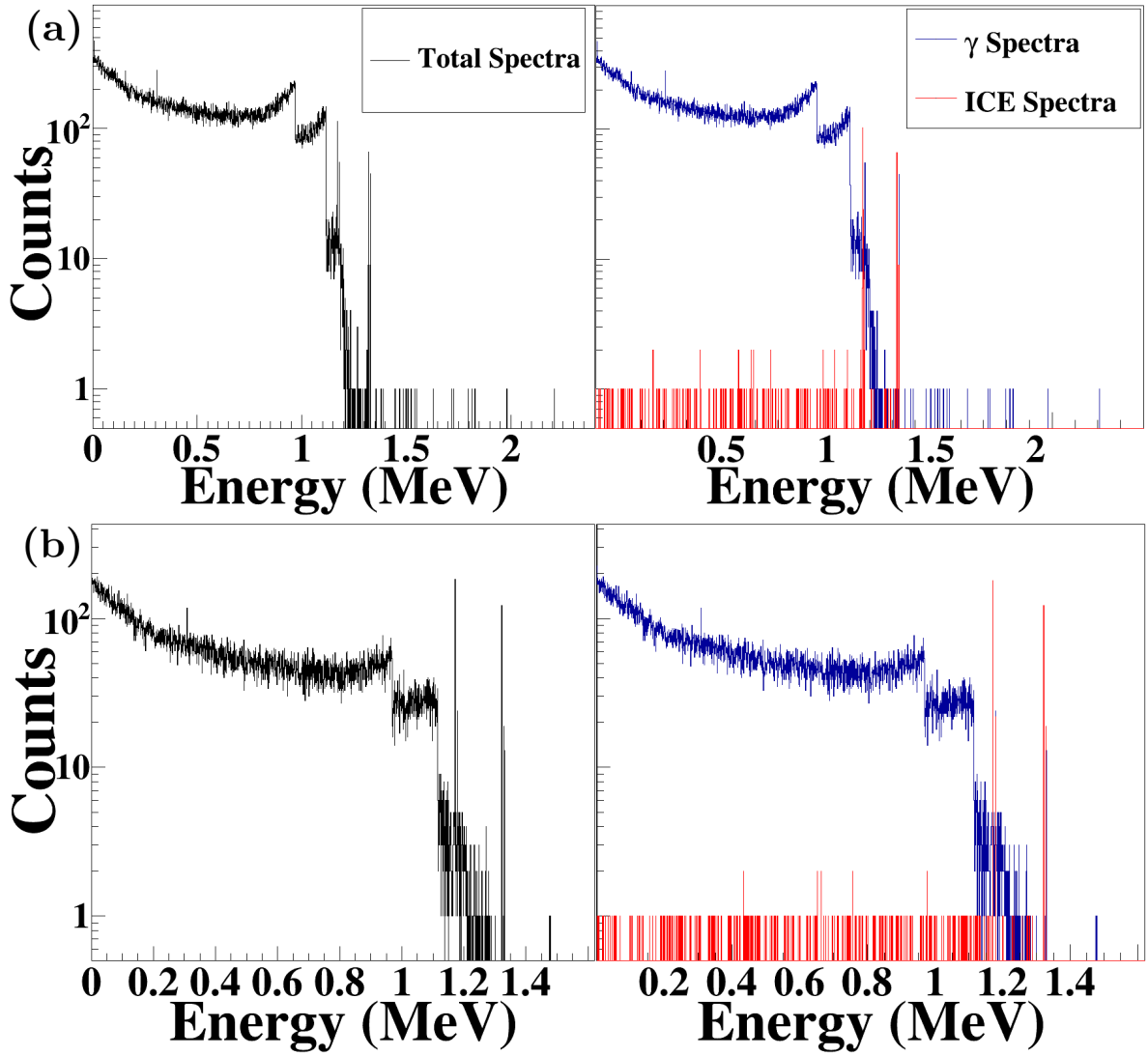


***Figure 5.5:*** *Simulated energy spectra of 20 million $^{60}$Co decays within the two different detectors. Each showing the electron and $\gamma$ rays contribution (right hand side) to the total spectra (left hand side): (a) with the PACES array, and (b) with the CEDAR design proposal with a sample magnetic lens.*

$^{56}$Co decays mostly via the $\beta^-$ channel producing $^{56}$Ni fed into 12 excited states of varying intensities. These states then de-excite through the emission of $\gamma$ rays and ICEs, in this region of the nuclear chart the more likely decay is again through $\gamma$ rays. The atomic electrons are very weakly bound with the $e_K$ and $e_L$ binding energies equal to 7.11 keV and ∼0.8 keV. For simplicity the simulation only includes the emission of electrons from the K and L orbitals.

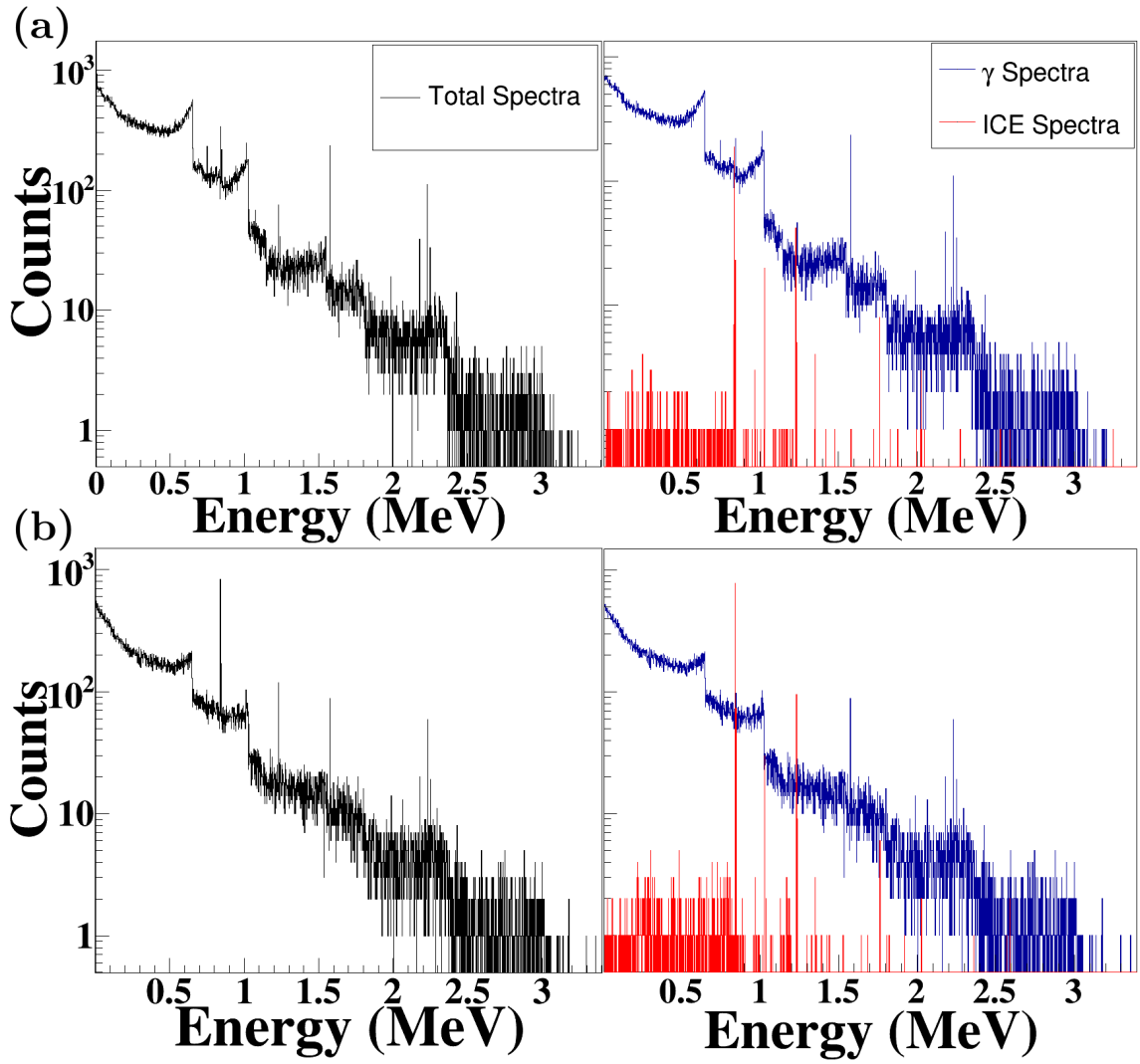


***Figure 5.6:*** *Simulated energy spectra of 20 million $^{56}Co$ decays within the two different detectors. Each showing the electron and $\gamma$ rays contribution (right hand side) to the total spectra (left hand side): (a) with the PACES array, and (b) with the CEDAR design proposal with a sample magnetic lens.*

# Chapter 6

# Systematics

An important part of this project was understanding how the shape of the magnetic lens affected the transmission of electrons through the lens. In order to accomplish this a selection of systematic studies was performed. The principle was to keep all but one variable constant, investigating the effect of the changing variable and then optimize accordingly. A combination of these optimized variables would produce the best design achievable. This chapter will discuss the results from these investigations.

## 6.1 Source Facing Cut

The magnetic lens includes a "cut" on the leading edge (or source facing edge). This "cut" is a critical part of this design, distinguishing it from previous spectrometer designs. The angle and depth of this cut has a large impact of the effectiveness of the magnetic lens. These are therefore two of the most important variables in the lens.

Figure 6.1 displays the results of studies into these two variables. The angular investigations suggests that the optimal angle for this cut lies somewhere between 20 and 50 degrees. Also displayed in the the figure is a movement in the minimum threshold energy as a function of this angle. At $\theta = 20$ degrees the threshold is down at $\sim$75 keV, as $\theta$ increases the threshold gradually increases until $\theta$ is equal to 60 degrees. At this point the threshold energy drops until at $\theta = 80$ degrees it is now at $\sim$25 keV, however, it must be said that at the efficiency available, the statistics are very low and so the efficiency may be inaccurate at this threshold.

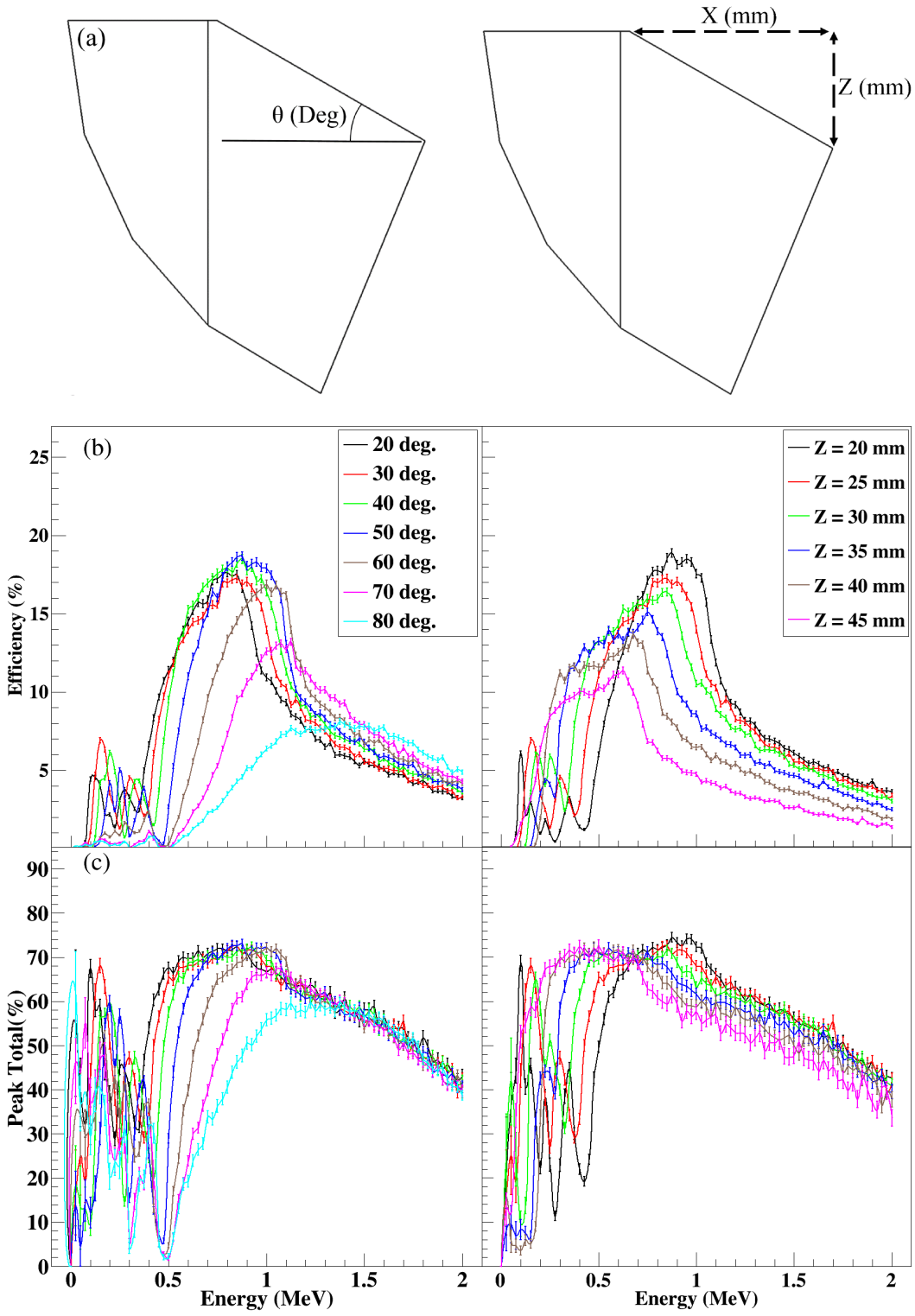


***Figure 6.1:*** *Systematics of the Source Facing Cut. On the left hand side is the angular systematics and on the right is the depth systematics, in each case all variables excluding the one in question are kept constant. Displayed from top to bottom: (a) A side view diagram depicting the variable in question, (b) The transmission efficiency from source to detector and (c) the peak/total as a function of electron energy.*

This angle causes such a dramatic shift in effectiveness for two main reasons. The first can be explained by the emitted angles of the electrons. Isotropically emitted, there is a distribution of angular emission for a given energy. This means for any given energy, more or less "bending" is required for successful transmission, which is dependent on the emission angle of that electron. A differing angular cut in the front edge of the magnet affects the position of entry of an electron (of a given emission angle) into the lens. This can put it onto a trajectory into the detector or not.

The second effect is due to the "fringe field" of the magnetic lens. The magnetic field lines do not traverse the space between magnets in a perfectly circular way and there is a component of the magnetic field that bends around each singular magnet at the extremities. The angle of the cut affects the specific directional components of these fields. The interaction between the electrons path through this fringe field and the directional component of the field can greatly change the final trajectory of the electron by adding another directional component to the acceleration through the lens.

It can also be seen that the depth of this cut effects the energy in which this region of peak efficiency occurs. This can be translated as the shallower the cut the larger "distance" spent (therefore longer "time") an electron of given energy spends within the magnetic lens. More bending of that given energy occurs, hence why it can be seen that the peak moves towards the higher energies. The lower energies are overly bent and therefore revolve within the magnetic lens without entering the detector. An effect on the threshold of these magnet lenses can also be seen. As the cut deepens from 25 mm to 40 mm the minimum energy can be seen to increase (from $\sim$90 keV to $\sim$150 keV). There is then a large drop down to 50 keV as the cut deepens to 45 mm.

A scaling of the peak total with the efficiency peaks can be seen in Figure 6.1 (c). As the peaks within the efficiency move, so do the peaks in the peak total curves. Unfortunately when the efficiency is low the peak total becomes unreliable due to low statistics within the spectra. From the left hand side, as $\theta$ increases the area of high peak total shifts towards higher energies. Conversely from the right hand side, as Z increases the area of high peak total shifts towards the lower energies.

## 6.2 Middle Plate

The middle plate of the magnet paddle design is a key variable. It affects the energy range over which the magnetic lens is effective by contributing to the strength of the magnetic field. As shown in Figure 6.2 the thicker the middle plate is the higher energy range at which the lens is efficient. The shape of the curve does not change in any obvious way, similarly the width of the peak efficiency is relatively unchanged. It can also be seen that the thicker the plate the higher the peak efficiency is at; for a thickness of 2.0 mm the peak efficiency is 13% while at 4.0 mm an efficiency of 17.5% is achieved. The electron peak total also follows a similar pattern as the middle plate is varied, above 0.5 MeV the curves are similar in the tail off with a small translation to higher energies. At energies below 0.5 MeV the peak total is unreliable due to low statistics but it can be seen that the peak total is a lot less stable, rapid changed occur over small energy differences, but the shapes are very similar.

As previously mentioned, a variable of this magnetic lens that makes it relatively unique is the "cut" in the source facing edge of the magnets. This is also true for the side of the magnetic lens that faces upstream towards the detectors. There is another "cut" as demonstrated in Figure 6.2. This cut is less important to the overall effectiveness of the magnetic lens. However, it allows for an extension to the depth of the magnetic lens. The limitation on the $\theta_{max}$ is based solely on the angle at which the detectors are placed. With the detectors placed at an angle of 22.5 degrees from the beam axis $\theta_{max}$ is set at 67.5 degrees. As displayed in the above figure, in comparison to other systematics investigated this has a very limited impact on the transmission efficiency of the magnetic lens.

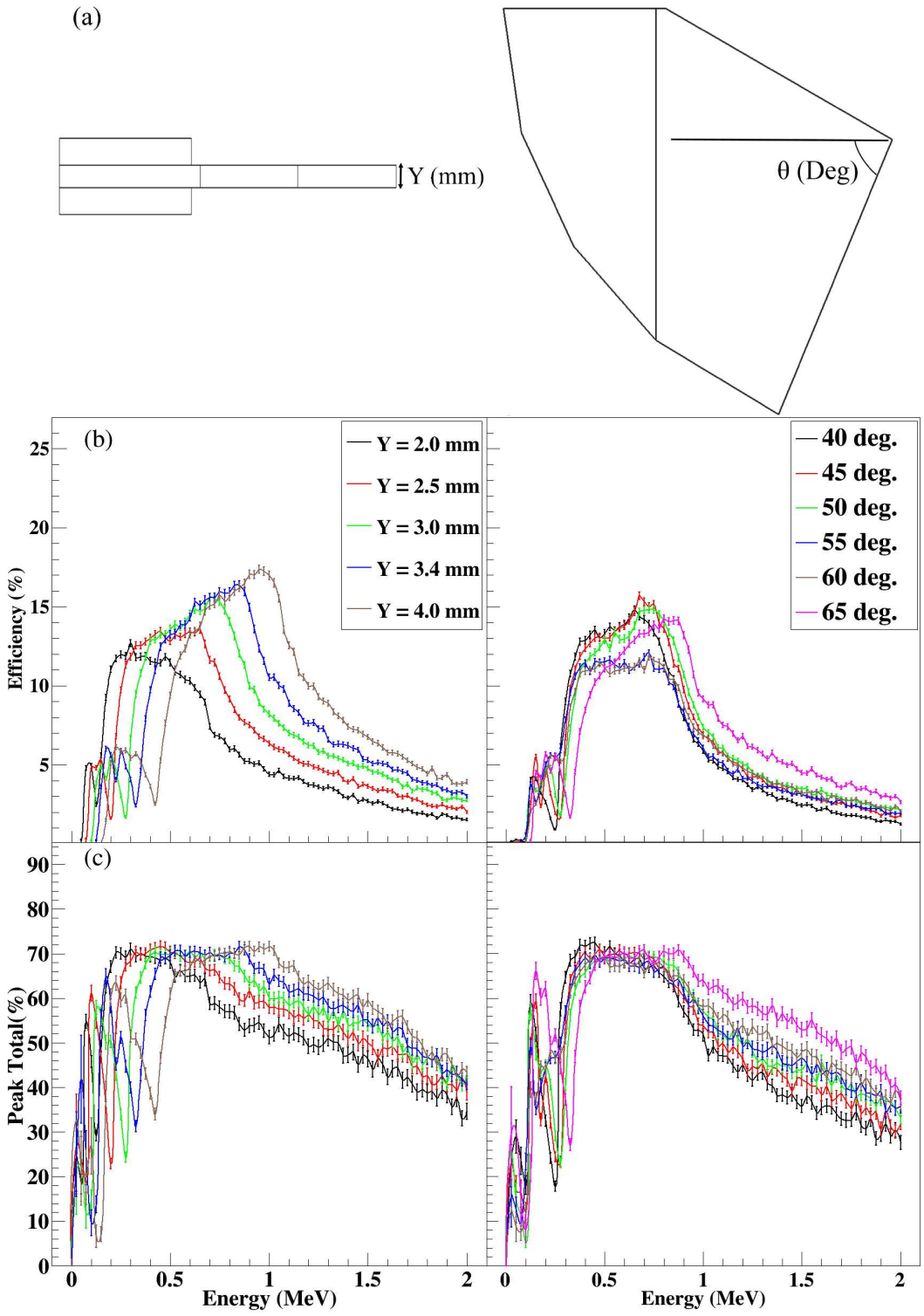


***Figure 6.2:*** *Systematics of the Middle Plate. On the left hand side is the middle plate thickness systematics and on the right is the angular systematics of the detector facing cut, in each case all variables excluding the one in question are kept constant. Also on the right hand side, as Z is varied X is also varied with the angle of the cut kept constant. Displayed from top to bottom: (a) A top (left) and side (right) view diagram depicting the variable in question, (b) The transmission efficiency from source to detector and (c) the peak/total as a function of electron energy.*

## 6.3 Paddle Variables

A major feature of this design is the "paddle" plates of the magnet. The large benefit of these plates is the increased width of the peak efficiency. This is one of the most important features for this design to be an effective modern electron spectrometer. It is therefore also important to understand how changing these plates affects the transmission of electrons. The effect the paddles have on this design is to increase the width of the peak efficiency at the expense of maximum peak efficiency. Peak efficient is important in order to detect the highest internal conversion electron peak within a given spectra. However, the experiments done with CEDAR will not have known transition energies and so being efficient over a large energy range allows for multiple transitions of varying energies to be seen and is therefore preferable. As a vacuum chamber within GRIFFIN, it will take a long time to change between different permanent magnet setups that could allow for many high peak efficiency magnet designs to be valuable, another reason a wide peak efficiency is important.

The above mentioned effect is very clear within Figure 6.3. On the left hand side the effect of increasing the size of the paddle on the efficiency and the peak total of internal conversion electron emission. Below 400 keV the increase in paddle length decreases the overall efficiency over this energy range. Above this, the clear effect of peak widening with increasing paddle length can be seen, with a small paddle length (X = 25 mm) the peak width is ∼300 keV whilst at larger lengths (X = 50 mm) the peak width is ∼1400 keV wide. The peak efficiencies are 22% and 11% respectively. It is also shown in this figure that peak total of the magnetic lens in general decreases as the paddle length increases. This can be explained from the increasing amount of material inside the chamber, this leads to more electron scattering.

When looking at the effect of the paddle thickness on the overall effectiveness of the magnetic lens, a similar conclusion can be drawn as the done for the length. Figure 6.3 shows that the peak efficiency width increases as the paddle is enlarged. When no paddle is added to the lens the middle plate is only the feature and alone has a peak efficiency width of ∼250 keV. However, at the largest paddle thickness investigated the peak efficiency width is more than twice as large at ∼600 keV. With no paddle the peak efficiency is 15% at 500 keV, adding in the paddle at small thicknesses creates a cost free gain in the peak efficiency of almost 6%. Further increasing the paddle leads

to a drop in efficiency but an increase in the peak efficiency width. At the extreme paddle thickness the peak efficiency is only at 13.5%.

This effect can be explained in a fairly simple way. At the leading edge of the paddle material the magnet is very thick relative to the middle plate (11.4 mm and 3.4 mm respectively) and so the magnetic flux circumventing the leading edge of the paddle is stronger than the flux from the middle plate at the same point. This causes a cancellation of the flux from the middle plate in this region and a new "fringe" field is caused in this region. So whilst increasing the paddle allows for some higher energy electrons to be transmitted into the detector, the fringe field around the paddle plates (which affects lower energy electrons more than higher energy) causes some of the lower energy electrons to not be transmitted. These are likely to scatter of the magnets themselves as the direction of the fringe field is such that it sucks electrons towards the magnet material.

In terms of the changes to the peak total as a function of these paddle variables, it can be seen that the changes to the paddle length makes a much larger impact than changes to the thickness. As the paddle length increases the peak total across the entire energy range of the simulation tends to decrease, except in the case of X = 55 mm between 1.2 MeV and 1.7 MeV where there is a small increase. This is exacerbated in the low energy region where the statistics are lower. As for the paddle thickness there is very little change in the overall peak total. A smaller thickness in general has a slightly higher value across the energy range but is within $\sim$5% across most energies. This is true for all except $<$150 keV where the threshold energy of the magnetic lens begins to have an effect.

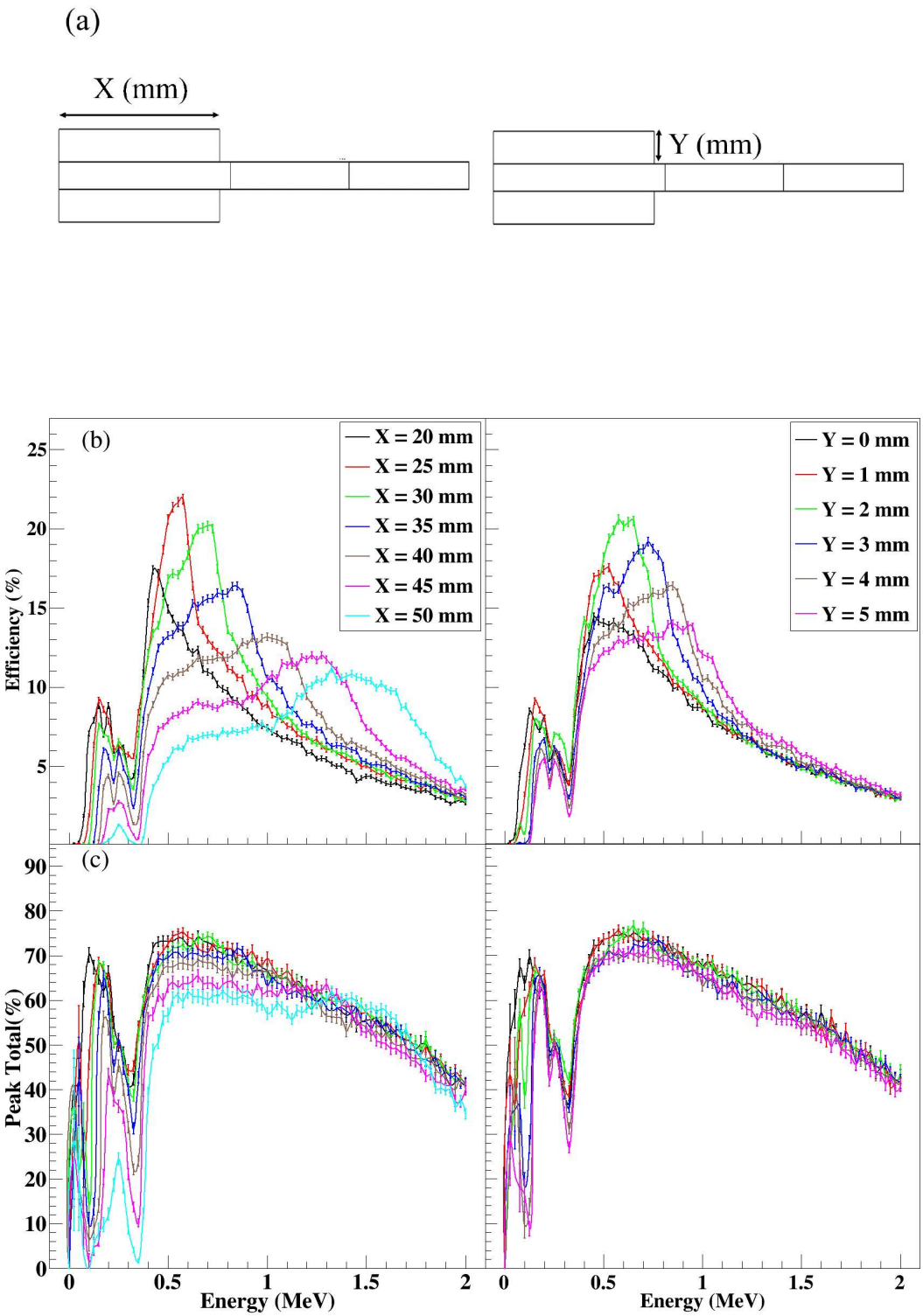


***Figure 6.3:*** *Systematics of the Paddles. On the left hand side is the paddle length systematics and on the right is the paddle thickness systematics, in each case all variables excluding the one in question are kept constant. Displayed from top to bottom: (a) A top view diagram depicting the variable in question, (b) The transmission efficiency from source to detector and (c) the peak/total as a function of electron energy.*

## 6.4 Magnetization Values and No. of Magnets

A cause for concern with this design is the uncertainty in the magnetization of the magnets. In order to determine the magnetization value of a given magnet the following is done. Firstly a permeance coefficient is calculated, based upon the shape and size of the magnet in question. In general the bigger the magnets the bigger this coefficient is. This permeance coefficient is the compared to a demagnetization curve, as shown in Figure 6.4. This gives values for a given temperature and material of the flux density, B, and the magnetic field, H. From the equation discussed in section 3.5, a magnetization value can then be calculated. The problem for this design is in determining the permeance coefficient. This is a complex value to calculate and currently only very simple shapes are readily calculable, such as squares or cylinders.

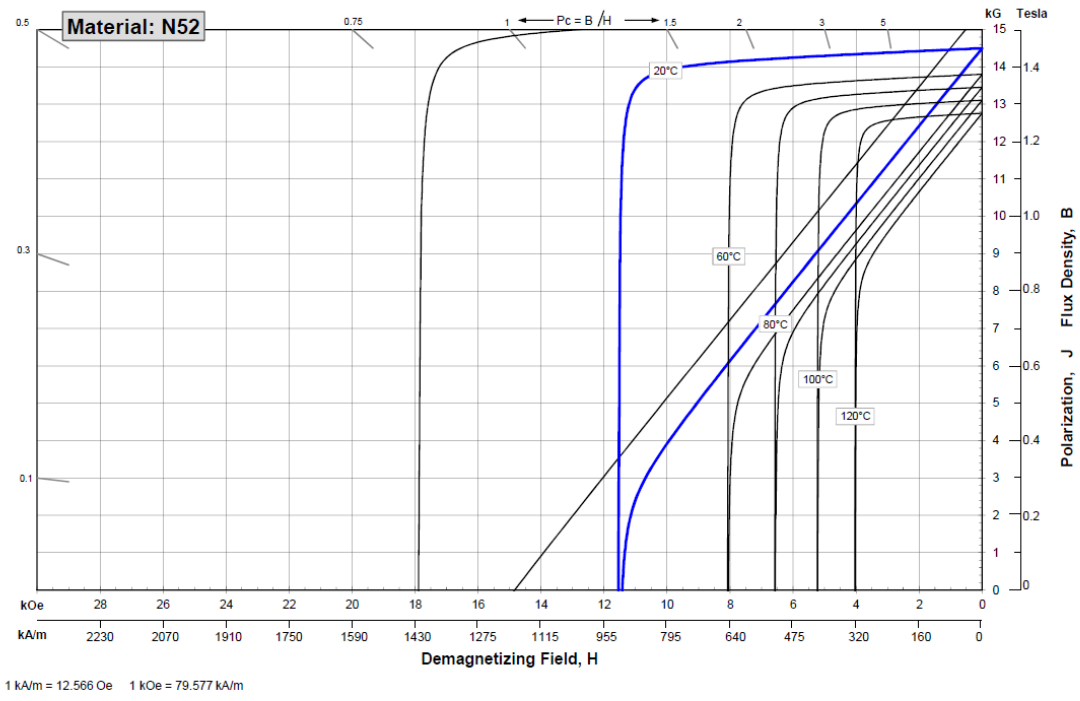


***Figure 6.4:*** *The demagnetization curve for N52 grade NdFeB magnets, as given by Arnold Magnetics [42]*

In reality, due to the sintering process of machining these magnets, no two magnets are made identical. This means that the before mentioned process is an estimate of the magnetization value at best. The only true way to determine the magnetization of a magnet design is to measure the field produced once made. Therefore, these simulations are reliant on choosing an arbitrary value for this magnetization value and then

understanding the overall effect of this value on the design. As TRIUMF has recently developed a similar detector (SPICE [12]) which uses magnets of a similar shape to the ones in use for this design, it was known that a magnetization value on the order of 900,000 A/m was a reasonable approximation for the purpose of these early designs. However, as previously mentioned the effect of changes to this value was needed.

Figure 6.5 shows the results from this investigation and also one in the effect of the number of magnets. Beginning with the magnetization value a clear effect is observed, with increasing magnetization value the shape of the efficiency curve is more or less unchanged. The main difference is an apparent translation towards a slightly higher energy, with an extra 50,000 A/m correlating to ∼100 keV shift. It can also be seen that in this investigation 900,000 A/m would represent an optimal value with in general the efficiency being a couple of percent higher than expected. This could be due to the other variables being somewhat optimized to this value as previously discussed. The same can be seen for the peak total where little change occurs except from a shift in the curve to higher energies.

On the other hand Figure 6.5 also displays the relatively large impact the number of magnets used in the lens makes on the effectiveness of the lens. The conclusion that more magnets equals an efficiency peak at higher energies can be drawn in a general sense. There is a complex relationship between the number of magnets and the width of the efficiency peak. Depending on how the width of the peak is defined it could be argued that the peak is widest with a full lens of 8 magnets, whilst it is clear that the peak is narrowest when only 4 magnets are used. What is interesting to note is that the configuration of the 6 magnet lens has an effect on the results observed. If the magnets are in the quadrants next to each other the efficiency is marginally higher between 850 keV and 1 MeV whilst it is slightly lower between 250 keV and 550 keV.

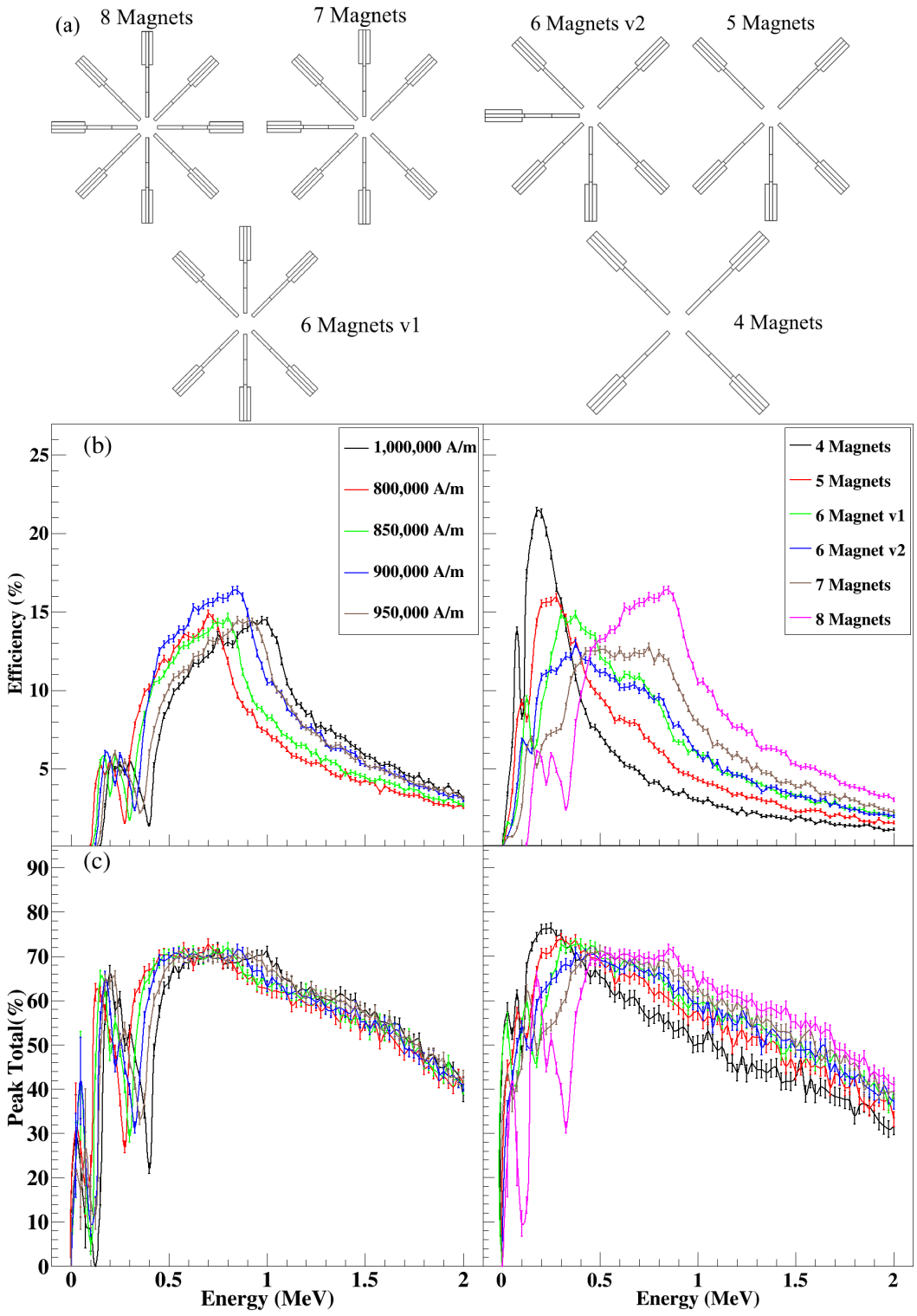


***Figure 6.5:*** *On the left hand side is the Magnetization value systematics and on the right the number of magnet systematics, both using the template design. Displayed from top to bottom: (a) Both the left and right hand side display the varying layout of the lens as the number of magnets is changed, (b) The transmission efficiency from source to detector and (c) the peak/total as a function of electron energy.*

There is an issue with having an asymmetric magnetic lens however. In the case of one of the Silicon Lithium detectors failing the efficiency of CEDAR would change dramatically and unpredictably. Each detector within the array is measuring energies with a different efficiency. With the asymmetric designs there are more energy regions of the observed minor peaks, these are due to the different regions of high efficiency within this array. These regions can not be observed in Figure 6.5 because they are hidden under the high efficiency regions of the other detectors within the array. These would become more apparent if detectors began to fail. This would be a large issue for an experiment if the failure of a detector occurred during an ongoing experiment, this would cause issues with post-experiment analysis. With a symmetric design this is not the case as each detector within the array makes up approximately 25% of the efficiency for a given energy and all of the detectors are recording the same energies equally. In the case of a failure with a symmetric design a simple scaling factor could be added to the efficiency calibrations in order to match the loss of a detector.

# Chapter 7

# Conclusion & Future Work

The key objective of this project was to begin the concept design for an internal conversion electron spectrometer to replace the PACES array in current use at TRIUMF. The aim being that the geometry of CEDAR would be optimized in order to observe the relevant physics with much reduced sources of background. The new geometry required must not hinder the facilities it would be coupled with (GRIFFIN & SCEPTAR) whilst being more efficient, be able to handle a higher count rate and have reduced sources of background when compared to PACES.

In a modern experiment it is important to make the most of the allotted "beam time", meaning that measuring $\gamma$ rays and ICEs from nuclear decay is a significant advantage. Using the GRIFFIN HPGe array to detect $\gamma$ rays whilst simultaneously measure ICES within the Si(Li) array of CEDAR fulfills this. This design fitting geometrically within the target chamber of GRIFFIN is a major accomplishment of this concept design. A significant issue of ICE spectroscopy is constraining detections to solely ICEs. In order to reduce background a photon shield optimized to attenuate $\gamma$ rays of 511 keV energy by 99.9% was designed. Whilst this does not remove the background from the $\gamma$ rays that scatter around the chamber it is still a significant reduction than in PACES.

Arguably the most difficult part of this was to design and prove the effectiveness of a complex magnetic lens, used for transporting electrons from a source into the array of detectors. It has been shown that multiple lenses of permanent magnets could be designed and optimized for a wide range of electron energies. In the future a series of generic lenses can be fabricated and made available to users. More importantly it

would possible to design a magnetic lens optimized towards a specific experiment if the criteria was not met by the generic lenses. Although this would add in more preparation towards and experiment, it has been shown that only small changes would be needed for this. This would be problematic for an experiment if the transition energies were not known, however, within an experiment lenses could be swapped in and out with differing energy ranges of efficiency.

The next step in the design of CEDAR will be to take the concept design into a fully functioning detector. The design will be expanded to include the support structures for the various components. This will most likely happen within the next year.

# Bibliography


[1] E.W. Blackmore. Operation of the TRIUMF (20-500 MeV) proton irradiation facility. In *Radiation Effects Data Workshop*, pages 1–5, 2000.

[2] L. Merminga J. Dilling, R. Krücken. In *ISAC and ARIEL: The TRIUMF Radioactive Beam Facilities and the Scientific Program*. Springer Netherlands, 2014.

[3] C.E. Svensson and A.B. Garnsworthy. The GRIFFIN spectrometer. *Hyperfine Interactions*, 225(1-3):127–132, 2014.

[4] A.B. Garnsworthy and P.E. Garrett. The $8\pi$ spectrometer. *Hyperfine Interactions*, 225(1-3):121–125, 2014.

[5] P. Kleinheinz, L. Samuelsson, R. Vukanović, and K. Siegbahn. A four-detector electron directional correlation spectrometer. *Nuclear Instruments and Methods*, 32(1):1 – 27, 1965.

[6] J.S. Dionisio, Ch. Vieu, E. Gueorguieva, M. Kaci, E.B. Kharraja, M.G. Porquet, C. Schück, J.M. Lagrange, M. Pautrat, W.R. Phillips, J.L. Durell, P.G. Dagnall, S.J. Dorning, M.A. Jones, A.G. Smith, B.J. Varley, J.C.S. Bacelar, W. Urban, T. Rzaca-Urban, A. Minkova, Th. Venkova, H. Folger, J. Vanhorenbeeck, and A. Passoja. Recent developments of multi e-$\gamma$ spectrometers. *Nuclear Instruments and Methods in Physics Research Section A: Accelerators, Spectrometers, Detectors and Associated Equipment*, 437(2-3):282 – 334, 1999.

[7] M. Luontama, J. Kantele, R. Julin, A. Passoja, T. Poikolainen, and M. Pylvänäinen. A combination intermediate-image magnetic plus Si(Li) electron spectrometer for in-beam experiments. *Nuclear Instruments and Methods*, 159(2-3):339 – 345, 1979.

[8] P.A. Butler, P.M. Jones, K.J. Cann, J.F.C. Cocks, G.D. Jones, R. Julin, and W.H. Trzaska. Electron spectroscopy using a multi-detector array. *Nuclear Instruments and Methods in Physics Research Section A: Accelerators, Spectrometers, Detectors and Associated Equipment*, 381(2-3):433 – 442, 1996.

[9] J. Pakarinen, P. Papadakis, J. Sorri, R.-D. Herzberg, P.T. Greenlees, P.A. Butler, P.J. Coleman-Smith, D.M. Cox, J.R. Cresswell, P. Jones, R. Julin, J. Konki, I.H. Lazarus, S.C. Letts, A. Mistry, R.D. Page, E. Parr, V.F.E. Pucknell, P. Rahkila, J. Sampson, M. Sandzelius, D.A. Seddon, J. Simpson, J. Thornhill, and D. Wells. The SAGE spectrometer. *The European Physical Journal A*, 50(3), 2014.

[10] B. Aengenvoort, W. Korten, H. Hübel, S. Chmel, A. Görgen, U.J. Van Severen, W. Pohler, R. Zinken, T. Härtlein, C. Ender, F. Köck, P. Reiter, D. Schwalm, F. Schindler, J. Gerl, R. Schubart, F. Azaiez, S. Bouneau, J. Duprat, and I. Deloncle. Conversion-electron gamma-ray coincidence spectroscopy of superdeformed 135nd. *European Physical Journal A*, 1(4):359–364, 1998. cited By 4.

[11] M.P. Metlay, J.X. Saladin, I.Y. Lee, and O. Dietzsch. The ICEBall: a multiple element array for in-beam internal conversion electron spectroscopy. *Nuclear Instruments and Methods in Physics Research Section A: Accelerators, Spectrometers, Detectors and Associated Equipment*, 336(1-2):162 – 170, 1993.

[12] S. Ketelhut, L.J. Evitts, A.B. Garnsworthy, C. Bolton, G.C. Ball, R. Churchman, R. Dunlop, G. Hackman, R. Henderson, M. Moukaddam, E.T. Rand, C.E. Svensson, and J. Witmer. Simulated performance of the in-beam conversion-electron spectrometer, {SPICE}. *Nuclear Instruments and Methods in Physics Research Section A: Accelerators, Spectrometers, Detectors and Associated Equipment*, 753(0):154 – 163, 2014.

[13] C.E. Svensson, P. Amaudruz, C. Andreoiu, A. Andreyev, R.A.E. Austin, G.C. Ball, D. Bandyopadhyay, A.J. Boston, R.S. Chakrawarthy, A.A. Chen, R. Churchman, T.E. Drake, P. Finlay, P.E. Garrett, G.F. Grinyer, G. Hackman, B. Hyland, B. Jones, R. Kanungo, R. Maharaj, J.P. Martin, D. Morris, A.C. Morton, C.J. Pearson, A.A. Phillips, J.J. Ressler, R. Roy, F. Sarazin, M.A. Schumaker, H.C. Scraggs, M.B. Smith, N. Starinsky, J.J. Valiente-Dobón, J.C. Waddington, and

L.M. Watters. TIGRESS: TRIUMF-ISAC Gamma-Ray Escape-Suppressed Spectrometer. *Journal of Physics G: Nuclear and Particle Physics*, 31(10):S1663–S1668, 2005. cited By 35.

[14] J. Andrzejewski, A. Król, J. Perkowski, K. Sobczak, R. Wojtkiewicz, M. Kisieliński, M. Kowalczyk, J. Kownacki, and A. Korman. Electron spectrometer for "in-beam" spectroscopy. *Nuclear Instruments and Methods in Physics Research Section A: Accelerators, Spectrometers, Detectors and Associated Equipment*, 585(3):155 – 164, 2008.

[15] J. Perkowski, J. Andrzejewski, Ł. Janiak, J. Samorajczyk, T. Abraham, Ch. Droste, E. Grodner, K. Hadyńska-Klęk, M. Kisieliński, M. Komorowska, M. Kowalczyk, J. Kownacki, J. Mierzejewski, P. Napiorkowski, A. Korman, J. Srebrny, A. Stolarz, and M. Zielińska. University of Lodz an electron spectrometer - a new conversion-electron spectrometer for "in-beam" measurements. *Review of Scientific Instruments*, 85(4):–, 2014.

[16] Jouni Suhonen. Beta Decay. In *From Nucleons to Nucleus*, Theoretical and Mathematical Physics, pages 157–204. Springer Berlin Heidelberg, 2007.

[17] S. Taverniet. *Experimental Techniques in Nuclear and Particle Physics*. Springer-Verlag, Berlin, Heidelberg, Germany, 2010.

[18] K.S. Krane. *Introductory Nuclear Physics*. John Wiley & Sons, 1988.

[19] M.F. L'Annunziata. *Radioactivity: Introduction and Early History*. Elsevier Science and Technology, Amsterdam, NLD, 2007.

[20] Roland J. Lombard, Charles F. Perdrisat, and Jean H. Brunner. Internal pair formation and multipolarity of nuclear transitions. *Nuclear Physics A*, 110(1):41 – 55, 1968.

[21] J. Kramp, D. Habs, R. Kroth, M. Music, J. Schirmer, D. Schwalm, and C. Broude. Nuclear two-photon decay in 0+âĘŠ0+ transitions. *Nuclear Physics A*, 474(2):412 – 450, 1987.

[22] D.C. Tayal. *Nuclear Physics*. Global Media, 2009.

[23] J.S. Basdevant and J.M. Rich. *Fundamentals In Nuclear Physics: From Nuclear Structure to Cosmology*. Springer, New York, NY, USA, 2005.

[24] J.M. Blatt and V.F. Weisskopf. *Theoretical Nuclear Physics*. Wiley, New York, NY, USA, 1952.

[25] E. L. Church and J. Weneser. Electric-Monopole Transitions in Atomic Nuclei. *Phys. Rev.*, 103:1035–1044, Aug 1956.

[26] T. Kibédi, T.W. Burrows, M.B. Trzhaskovskaya, P.M. Davidson, and C.W. Nestor Jr. Evaluation of theoretical conversion coefficients using BrIcc. *Nuclear Instruments and Methods in Physics Research Section A: Accelerators, Spectrometers, Detectors and Associated Equipment*, 589(2):202 – 229, 2008.

[27] E. L. Church, M. E. Rose, and J. Weneser. Electric-Monopole Directional-Correlation Experiments. *Phys. Rev.*, 109:1299–1306, Feb 1958.

[28] T. Kibédi, G.D. Dracoulis, A.P. Byrne, and P.M. Davidson. Low-spin non-yrast states and collective excitations in 174os, 176os, 178os, 180os, 182os and 184os. *Nuclear Physics A*, 567(1):183 – 236, 1994.

[29] G.Bertolini and A. Coche. *Semiconductor Detectors*. North-Holland Publishing Company, 1968.

[30] G. F. Knoll. *Radiation Detection and Measurement*. Wiley, New York, NY, USA, 2010.

[31] R. Evans. *The Atomic Nucleus*. McGraw-Hill Companies, New York, 1955.

[32] A. Beiser. *Concepts of Modern Physics*. McGraw-Hill Companies, New York, 2003.

[33] G.V. Pavlinsky. *Fundamentals of X-ray Physics*. Cambridge International Science Publishing, 2008.

[34] J. Lilley. *Nuclear Physics - Principles and Applications*. Wiley, New York, NY, USA, 2001.

[35] J.M.D. Coey. *Magnetism and Magnetic Materials*. Cambridge University Press, Cambridge, UK, 2009.

[36] Buschow K. H. J and F. R. De Boer. *Physics of Magnetism and Magnetic Materials*. Kluwer Academic Publishers, New York, NY, USA, 2003.

[37] S. Agostinelli and J. Allison et al. Geant4 - a simulation toolkit. *Nuclear Instruments and Methods in Physics Research Section A: Accelerators, Spectrometers, Detectors and Associated Equipment*, 506(3):250 – 303, 2003.

[38] Comsol Multiphysics. `http://www.comsol.com`.

[39] *Comsol Multiphysics User Guide*. Comsol, 2005.

[40] William L. Dunn and J. Kenneth Shultis. 1 - introduction. In William L. Dunn and J. Kenneth Shultis, editors, *Exploring Monte Carlo Methods*, pages 1 – 20. Elsevier, Amsterdam, 2012.

[41] ROOT : Data Analysis Framework. `https://root.cern.ch/`.

[42] Arnold magnetics website. `http://www.arnoldmagnetics.com/en-us/Products/Neodymium-` 2015.